8-5-2020

Facile Synthesis of Bio-templated Tubular Co3O4 Microstructure and its Electrochemical Performance in Aqueous Electrolytes

Deepa Guragain

FACILE SYNTHESIS OF BIO-TEMPLATED TUBULAR CO$_3$O$_4$ MICROSTRUCTURE AND ITS ELECTROCHEMICAL PERFORMANCE IN AQUEOUS ELECTROLYTES

by

Deepa Guragain

A Thesis

Submitted in Partial Fulfillment of the

Requirements for the Degree of

Master of Science

Major: Physics and Materials Science

The University of Memphis

August 2020

DEDICATED TO MY FAMILY

Acknowledgment

I would like to thank my advisor Professor Sanjay R. Mishra of the University of Memphis, for all invaluable advice, guidance, input, and supervision throughout this research work. His inventive research ideas, motivation, and friendly behavior encouraged me during my MS study. I would like to thank Professor Dr. Muhammad S. Jahan and Dr. Thang Ba Hoang for agreeing to be my thesis committee members despite their extremely busy schedules. I would also like to acknowledge Dr. Bostard Gustav for his kind help and technical support in many ways throughout my study period. Special thanks to Dr. Ram Gupta from Pittsburg State University, Pittsburg, Kansas, who helped with the electrochemical measurement of the prepared sample. I hereby also sincerely thank the graduate course teachers Dr. Sanjay R. Mishra, Dr. Mohamed Laradji, Dr. Xio Shen, Dr. Chenhui Peng from the department of physics and material science and Dr. Gladius Lewis from the engineering department. I would like to thank the administrative associate, Ms. Courtney R. Paulino, for providing her valuable support.

Finally, I would like to express my sincere gratitude to my family members and friends who support me in making my thesis successful. Continuous support and encouragement from family allowed me to complete the research and supported me to study abroad. It will hold a special place in my heart forever. Mainly thanks to my husband for his unconditional supports and motivation, which work as mental strength during a difficult time.

Abstract

Template-assisted facile synthesis of tubular Co_3O_4 microstructures and its electrochemical performance was studied to understand its use as a potential electrode material for supercapacitors. Tubular porous Co_3O_4 microstructures were synthesized using cotton fibers as bio-template. The as-obtained templated Co_3O_4 structure inherits the morphology and microstructure of cotton fiber. The electrochemical performance of the electrode made up of tubular Co_3O_4 structure was evaluated in 3M KOH, NaOH, and LiOH aqueous electrolytes. The large-surface-area of tubular Co_3O_4 microstructure has a noticeable pseudocapacitive performance with a capacitance of 401 F/g at 1 A/g and 828 F/g at 2 mV/s, a Coulombic efficiency averaging ~100%, and excellent cycling stability with capacitance retention of about 80% after 5,000 cycles. Overall, the tubular Co_3O_4 microstructure displayed superior electrochemical performance in 3M KOH electrolyte with peak power density reaching 5,500 W/kg and energy density exceeding 22 Wh/kg. The superior performance of the tubular Co_3O_4 microstructure electrode is attributed to its high surface area and adequate pore volume distribution, which allows effective redox reaction and diffusion of hydrated ions. The facile synthesis method can be adapted for preparing various metal oxide microstructures for possible applications in catalysis, electrochemical, sensors, and fuel cell applications.

Keywords: Biotempleted, Co_3O_4, electrochemistry, supercapacitance, specific capacitance

TABLE OF CONTENTS

LIST OF FIGURES

CHAPTER 1

INTRODUCTION

1.1 Introduction to Energy Storage Devices

In this twenty-first century, the energy issue has become one of the greatest challenges due to growing energy consumption with a growing population and technology development. Access to electricity become a basic need in today's lifestyle; in this regard, energy storage plays a significant role. There is a high demand for the development of cost-effective, environmentally benign, sophisticated, clean, and renewable energy storage devices due to the depletion of fossil fuels and increasing environmental concerns [1]. The most two prominent energy storage devices are electrochemical capacitors and batteries [2]. Furthermore, Li-ion batteries (LIBs) can achieve energy densities as high as (120-150 Wh/kg$_{-1}$), due to slow power delivery (100- 1000 W/kg$_{-1}$) and kinetics-limited charge/discharge LIBs hinders their practical application for energy storage systems [3]. On the other hand, researchers are actively working on electrochemical capacitors (ECs) due to the capability of power uptake and delivery effort within a second. In ECs, energy densities are lower than batteries; hence ECs are in need of considerable effort to increase their energy density without sacrificing the high-power capability.

Electrochemical capacitors have a tendency to perform many thousands of times higher power density than lithium-ion batteries and much larger energy density compared to conventional capacitors. Hence, supercapacitors are a promising candidate to meet increasing power demands for energy storage systems [4]. Supercapacitors have become a dominating candidate for next-

generation power devices due to their high-power density, fast charge-discharge rate, sustainable cyclic life (up to millions of cycles), and excellent cycle stability [5].

The discussion for major energy storage devices such as capacitors, batteries, fuel cells, and electrochemical supercapacitors are explained below;

1.1.1   Capacitors

A capacitor consists of two conducting parallel metal plates separated by a vacuum or dielectric material. In other words, it is a passive electrical device with the two-terminal electrical elements, which stores energy as a charge in the electric field between two conducting plates called electrodes. When a capacitor is connected to direct current (DC) circuit, it charges up to its supply voltage and the current flow block by an insulating dielectric material. On the other hand, when a capacitor is connected with alternating current (AC) circuit, the flow of current appears to pass straight through the capacitor with negligible resistance. In metal plates capacitor, there are two types of electrical charges where positive (+ve) charges are in the form of proton and negative (-ve) charge in the form of the electron. As a DC voltage is connected across a capacitor, the positive charge quickly accumulates on one plate and negative charge on another plate. Finally, the plates remain charge neutral and a potential difference established between two plates. Due to the presence of an insulator between two parallel plates, after reaching steady-state conditions, no more electric current can flow from one plate to another. This current continues to flow until the voltage across both plates becomes equal to the applied voltage. This point is called the capacitor fully charged state. Charge $Q= |Q_+| + |Q_-|$ and potential V related to each other through proportionality constant C,

$$Q = CV \quad \ldots\ldots (1.1.1)$$

Here C is proportionality constant. This refers to its capacitance and provides a measurement of the amount of charge necessary to induce a specified potential between the plates. The magnitude of capacitance is independent of the charge accumulated across the plates in a linear capacitor.

$$C = \frac{Q}{V} \quad \ldots\ldots (1.1.2)$$

$$C = \frac{\varepsilon . A}{d} \quad \ldots\ldots (1.1.3)$$

Here ε is the dielectric constant of dielectric materials, A is electrode surface area, and d is the distance between two planar electrodes. Capacitance C is measured in farads (F) where 1F=1 coulomb/volt (C/V).

Generally, the capacitors can release the stored charge very fast because capacitors have a low internal resistance that results in a high power due to which it cannot store much energy. The charge gets accumulated on the surface of the plates, which are isolated with the insulating dielectric layer; thus, an electric field is generated that allows the capacitor to store energy.
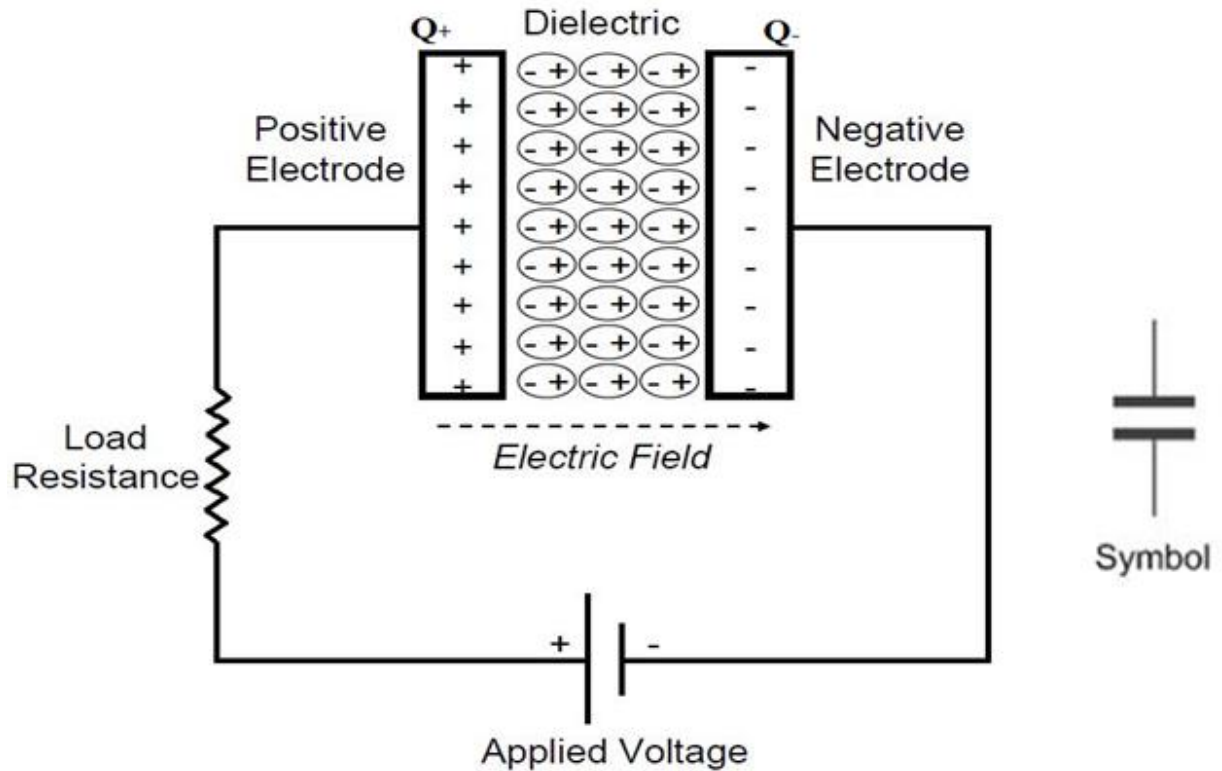
Fig.1.1.1 Schematic illustration of the electrostatic capacitor (conventional capacitors) which consists of two conducting plates separated by a dielectric.

The characteristics of the performance of an energy storage device are determined by energy density and power density. The energy density (E) determines the capacity to store charge, which is defined as energy per unit mass. Power density (P) indicates the rate of conversion of stored energy, and this is defined as power per unit mass.

$$E = \frac{1}{2}CV^2 \quad \text{... (1.1.4)}$$

and

$$P = \frac{E}{t} \quad \dots (1.1.5)$$

Here, t is the time required to discharge the capacitor.

The amount of stored energy (W) depends on the amount of charge that is stored on the capacitor's electrodes. The formula that describes this relationship is:

$$W = \frac{1}{2}\frac{Q^2}{C} = C * V^2 \dots\dots\dots\dots\dots\dots (1.1.6)$$

Where W is the energy stored on the capacitor that is measured in joules, Q is the amount of charge stored on the capacitor, C is the capacitance, and V is the voltage across the capacitor. As seen from the above equation, the maximum amount of energy that can be stored on a capacitor depends on the capacitance as well as the maximum rated voltage of a capacitor.

Generally, the electrostatic capacitors have a very higher power density higher than 5000 W/kg and a very low energy density of the order of 0.01-0.05 Wh/kg. In capacitors, the energy density low, less than 1% of supercapacitor and lesser than batteries. On the other side, capacitors have power density higher than batteries, often higher than a supercapacitor. Hence, in conclusion, the capacitors are able to deliver or accept high currents and can be charged and discharged rapidly but cannot store a large amount of energy.

1.1.1.1 Charging and Discharging a Capacitor

When a capacitor is connected to a DC power supply, current flows through the circuit and charges are transported from one plate to another, and they assume opposite polarities. Overall, the two plates together are electrically neutral. With the increase in the accumulation of charges

5

the potential difference between the plates increases. This is the charging phase. The current that flows through the circuit starts from a maximum and falls to 0 once the capacitor is fully charged. During this period, the voltage begins at 0 and rises to a potential difference of V depending on the medium between the plates and their geometry.

In the discharging phase, the capacitor is connected across a load. Current flows through the circuit leading to a decrease in the potential difference between the plates as the stored charges are dispersed, and the plates individually attain electrical neutrality. Variation of the current and voltage with time for the charge and discharge phases are present in Figure 1.1.1.1.1.

Figure 1.1.1.1.1: Variation of voltage and current with time during charging and discharging of a capacitor [6].

1.1.2 Batteries

A battery is a device that stores energy and makes it available in the form of electrical energy. A battery converts chemical energy into electrical energy. In batteries, the charge transfer takes place through a redox or Faradaic reaction on cathode and anode. In the ideal case, the potential difference of batteries remains constant during the reaction or charge-discharge process. Batteries contain electrochemical cells with two electrodes; one is anions containing negative charge ions, and second is cations containing positive charge ions, and these are connected by conductive electrolyte, as shown in figure 1.1.2.1. The chemical reaction produces an electron on the anode, which produces a potential difference between anode and cathode. Hence, the electron tries to move towards positive charge cathode, but electrolyte does not allow this. When anode and cathode connected by conducting wire, electrons get a path to flow towards the cathode, and hence discharge takes place. Batteries are of two types:

1. Primary batteries (Disposable batteries): Primary batteries are for single uses, and hence these are unable to recharge. As a result, they are not able to return in their original forms. Examples are disposable battery use in remote, clock, zinc-carbon and alkaline batteries, etc.

2. Secondary batteries (Rechargeable batteries): Rechargeable batteries can be recharged by using electric current. In these batteries when external electric current connects the flow of electrons changes their directions and recharge the battery again. Hence the charging and discharging process governed by the transportation of anions and cations. Examples

of rechargeable batteries are Hybrid (NiMH), nickel-zinc (NiZn), lead-acid, Li-ion batteries, etc.
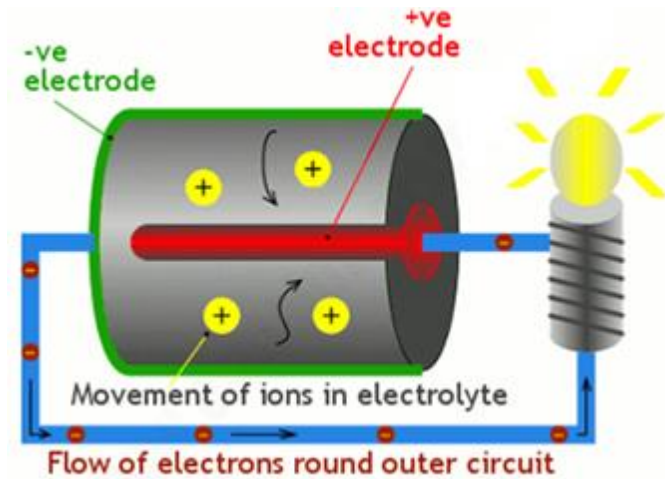
Figure 1.1.2.1: Schematic illustration for the working principle of batteries [7]**.**

Lithium-ion batteries (LIB) are very popular among all rechargeable batteries. LIB can have higher energy density (120-150 Wh/Kg), portability, very low memory effect, low self-discharge, and moderate weight [8]. In LIB, the cathode is made by intercalated lithium compounds, for example, iron phosphate, cobalt oxide, manganese oxide, and nickel oxides. Furthermore, the anode is made by graphite and other carbon materials. In LIB during charging, ions move from a positive electrode (cathode) to a negative electrode (anode) via the electrolyte. Li_+ ions easily can pass through the electrolyte, but electrons are not allowed to pass from the electrolyte, and hence they reach the anode through an external circuit. Again, during discharge, Li_+ ions move back to the cathode via electrolyte and electrons by an external circuit. A common example of LIBs is $LiCoO_2$, $LiMn_2O_4$, Li_2MnO_3, etc.

Fig.1.1.2.2: Schematic of a Li-ion battery [11].

A fundamental limitation of battery is low power density due to the slow chemical reaction and slow bulk diffusion, which make it hard to improve upon their power density characteristics.

1.1.3 Fuel Cells

Fuel cells convert the chemical energy completely (100%) into electrical energy from the fuel through the chemical reaction of positively charged hydrogen ions with oxygen or another oxidizing agent (electron acceptor). Fuel cells generate electricity from the external fuel supplied. The fuel cell technology is a clean, economical, and reliable solution for the power source due to the absence of any intermediate combustion steps where these produce water as a harmless byproduct. Furthermore, fuel cells show higher energy up to 500 Wh/Kg, but it has limited power density [9]. A fuel cell has electrodes as a cathode (+ve)

and anode (-ve) in the presence of an electrolyte. The most commonly used electrolytes are an aqueous alkaline solution, polymer membrane, and ceramic oxide. Fuel cell requires a continuous source of fuel and oxygen or air to sustain the reaction. The hydrogen is used as a catalyst to oxidize, which turns the fuel into a positively charged ion and negatively charged electron. Fuel membrane only allows positive ions to flow from the anode to cathode and act as an insulator for electrons. Hence, the positive hydrogen ions move towards cathode via a fuel cell and electron towards opposite ion movement through the wire and, as a result, electric current produce in electrolyte [10]. During this process, the ions (H_+) get reunited with the electrons at the cathode for the stability of the system, and they both together react with the third chemical, usually oxygen, to form water. The chemical reaction for this is;

Anode reaction: $H_2 \longrightarrow 2H_+ + 2e_-$

Cathode reaction: $\frac{1}{2}O_2 + 2H_+ + 2e_- \longrightarrow H_2O$

Total reaction: $H_2 + \frac{1}{2}O_2 \longrightarrow H_2O$
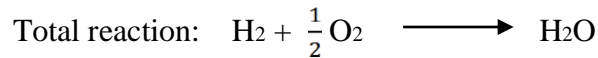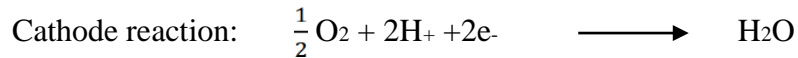
There are many types of fuel cells, such as alkali, molten carbonate, phosphoric acid, proton exchange membrane (PEM), and Solid oxide fuel cells. Below is the sketch for proton exchange fuel membrane:
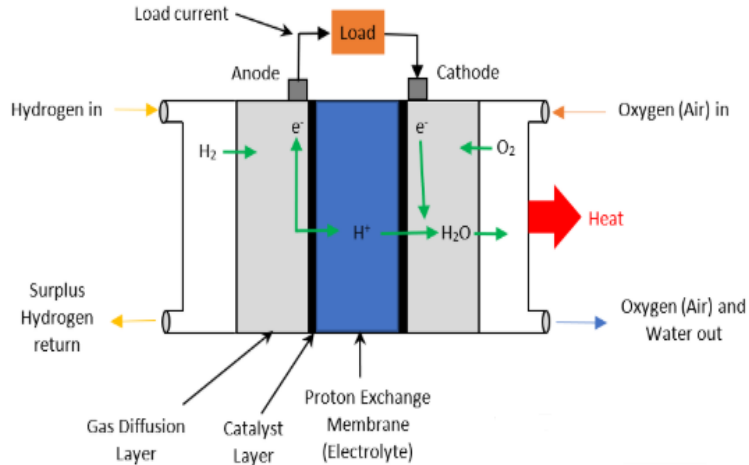
Fig.1.1.3.1 Schematic of a proton exchange membrane fuel cell (PEM) [11].

1.1.4 The Electrochemical Supercapacitors (ECs)

An ideal system would have a large energy density and a large power density. Due to the slow power delivery and the urgent need for higher power energy storage systems, the batteries and fuel cells have been replaced by the electrochemical supercapacitors. Researchers are focused on improving the increase in the energy density of ECs instead of increasing the power density of batteries. ECs are classified into three types 1) electrochemical double-layer capacitors (EDLCs), i.e., nonfaradaic and 2) Pseudocapacitors (PCs), i.e., faradic 3) hybrid capacitor which involves both faradic and non-faradic process for charge storage. The division is based on their mechanism of charging and discharging process.
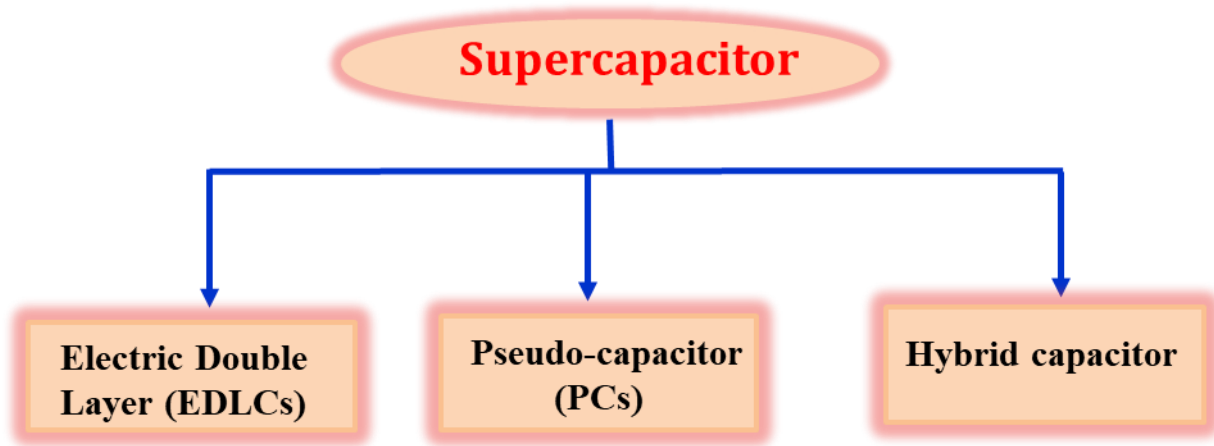
Fig.1.1.4.1 Schematic for type of supercapacitor

1.1.4.1 Electric double-layer capacitor (EDLCs)

Electrochemical double-layer capacitors have two electrodes having higher surface areas usually made by activated carbon, a separator that is ionically connected to each other via the electrolyte. When an external field (voltage) is applied to the EDLCs device, the ions of electrolyte solution diffuse across separator and get into the pores of the electrode. Due to applied voltage in both electrode there produce electrical double layer. This electrical double layer is a common boundary of opposite charges between a solid electrode and adjacent liquid electrolyte, which is called the Helmholtz double-layer [12]. The electrode materials having porosity can provide higher surface area, and hence it increases the capacitance value. Furthermore, due to the higher surface area, it creates a very short distance between electrode and electrolyte, which again increases the capacitance value.
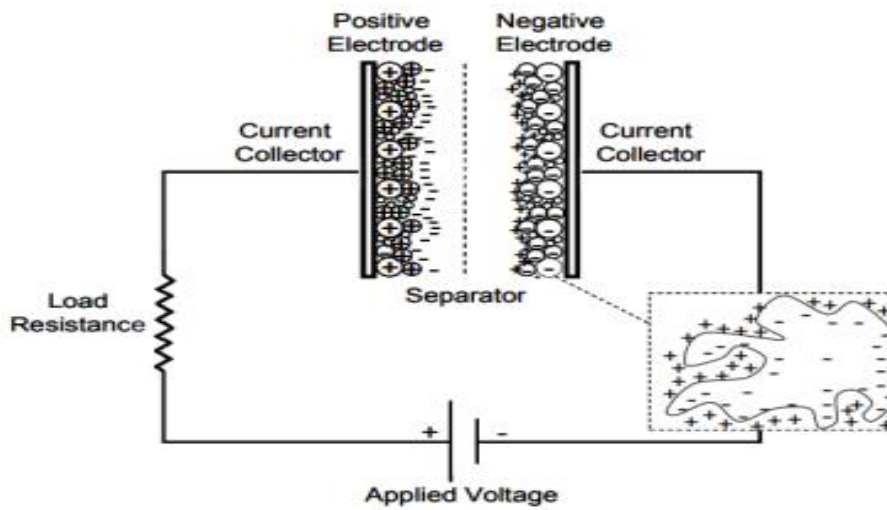
Fig.1.1.4.1 (a) Schematic of an electrochemical double layer capacitor (EDLC) [13].

During the charging process, when a voltage is applied, each electrode attracts ions of the opposite charge. Hence, corresponding opposite charge ions from electrolyte collect on the surface of two electrodes and there build up a charge in the electric double layer. During the discharging process, as added external load electron starts to flow from the external path, and no more ion gets strongly attract by electrode [14]. As a result of this ion starts to distribute through the electrolyte.
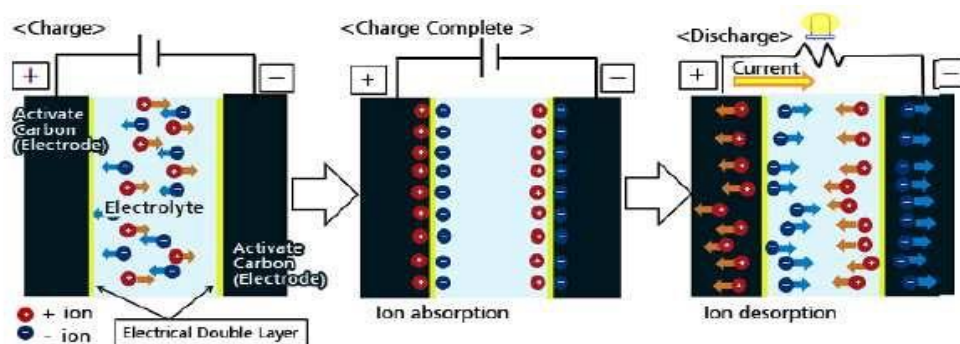
Fig. 1.1.4.2 (b): Charging and discharging phase of EDLCs
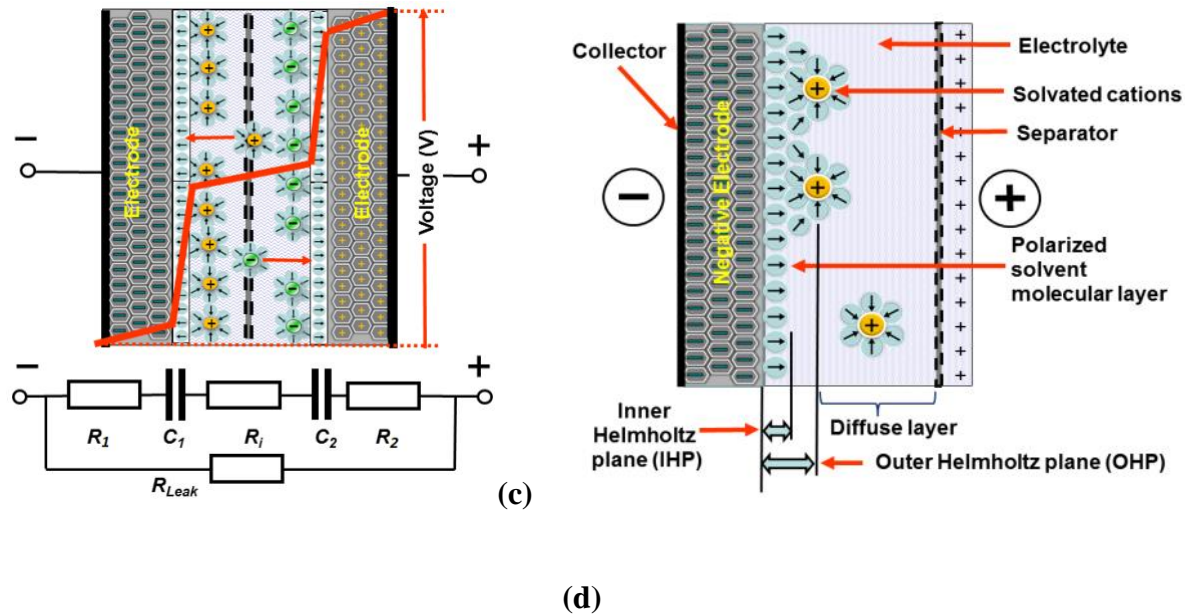
Fig. 1.1.4.3 (c): Voltage distribution across a charged EDLCs and the equivalent electrical circuit **(d):** Model illustrating the double layer capacitance [15]

Fig. 1.1.4.3 (c) shows the voltage distribution across a cell of charged EDLCs, and below is the equivalent electrical circuit. Hence, there is a capacitance associated with charge separation towards both electrodes. This gives two capacitances C_1 and C_2 connected in series, as shown in Figure 1.1.4.3 (c). The series resistance R_1 and R_2 are the resistance offered at collectors, and internal resistance R_I corresponds to ion movement within the electrolyte. A single cell of the EDLCs has two capacitors connected in series, and hence the net capacitance is the series sum of the capacitance at both the electrodes. Figure 1.1.4.3 (d) explains the three-layer of double-layer capacitance, which considers three planes;

- Inner Helmholtz plane (IHP)
- Outer Helmholtz plane (OHP) (Stern layer)

- Diffuse Layer

The solvent used for electrolytes is generally; water or organic liquids. The dipoles' presence in the solvent molecules interacts with the charged electrode's surface and orient with the oppositely charged end at near the electrode surface. The solvent molecule surrounds the electrolyte ions. IHP is made up of a monolayer of solvent molecules forming dielectric medium between opposite charges (of electrode and electrolyte ions), and hence IHP has a thickness of a single molecule layer. In the case of OHP, it extends from the center of the charged ion to the electrode surface. The diffuse layer is in the bulk solution. Figure 1.1.5.4 (e) depicts the variation of the potential across the double layer and in the diffuse layer.
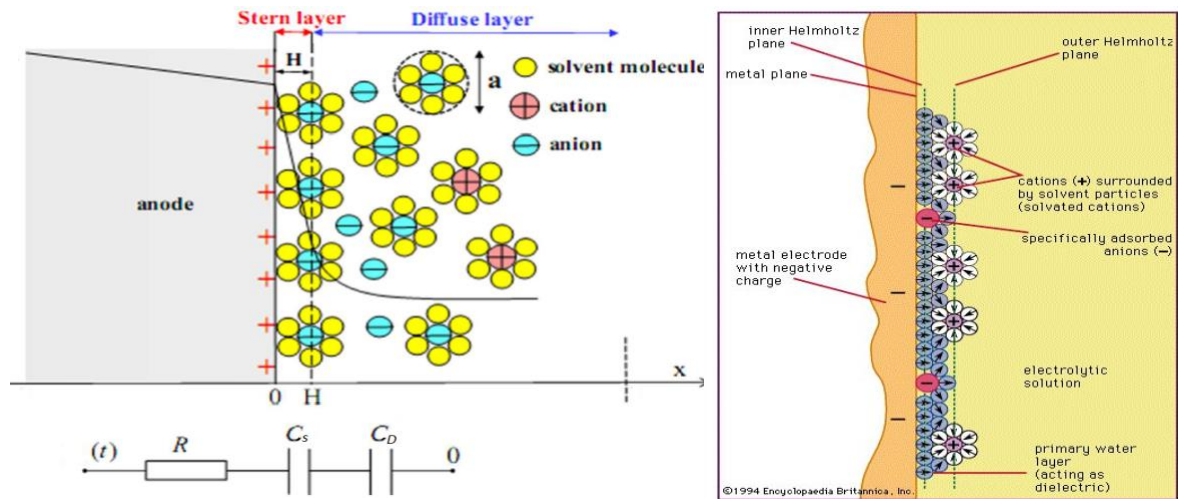
(e)

Figure 1.1.4.4 (e) Electrical circuit describing the split in the capacitance between the Stern layer and the diffuse layer with an accompanying illustration [16]

15

The double-layer capacitance is made up of capacitance of the Helmholtz plane/Stern layer and capacitance of the diffuse layer as a series connection, as illustrated in Figure 1.1.4.4 (e) lower part. C_s is the capacitance of the Stern layer and C_D, the capacitance of the diffuse layer.

1.1.4.2 Pseudocapacitors (PCs)

Pseudocapacitor is a faradic redox reaction based electrochemical capacitor. Pseudocapacitor has greater energy density than EDLCs, so, it is discovered to overcome the limitation of EDLCs. In PCs, the charging and discharging process occurs due to the adsorption of ions at the electrode/electrolyte interface as well as the faradic redox reaction between electrolyte and electrode surface. The PCs take advantage of both faradic and non-faradic charge accumulation. In this electron transfer between electrodes through redox reaction and parallelly charge stored due to the double layer effect.
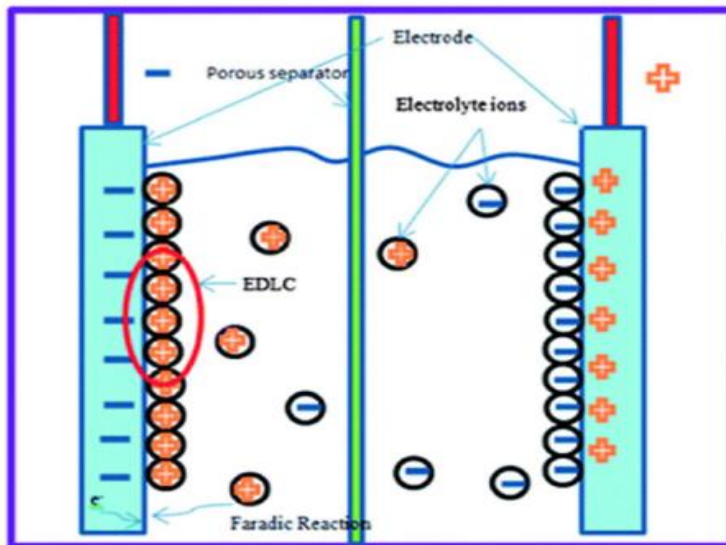
Fig.1.1.4.2.1 Schematic of a pseudocapacitor showing the adsorption of ions at the electrode/electrolyte interface from both faradic and non-faradic charge accumulation [17].

According to Conway (1999), the charge storing mechanism of pseudocapacitors is similar to that of batteries [18]. The capacitance of PCs is voltage-dependent. The capacitance obtained from PCs could be ten times larger than that of EDLCs.

1.1.4.2.1 Types of Pseudocapacitance

Pseudocapacitance is characterized by two-dimensional or near two-dimensional processes in storing charge. Pseudocapacitance results from three different mechanisms;

(a) Underpotential Deposition (UPD)

Underpotential deposition occurs when metal ions form an adsorbed monolayer (s) at a different metal surface above their redox potential [19]. UPD provides a precise means for quantitatively and reproducibly controlling coverage in the sub-monolayer to monolayer regime [20]. The monolayer is formed on electrode material at a potential more than the equilibrium potential of liquid. Examples of lead (Pb) on the gold (Au) surface occurs from the UPD deposition mechanism.

(b) Redox Pseudocapacitance

In redox pseudocapacitance, the charge transfer takes place between electrode and electrolyte by redox (reduction-oxidation) reaction, which is faradic in nature. Reduction occurs when electrons are accepted, and the oxidation state gets lowered. On the other hand, oxidation occurs when an electron is released, and the oxidation state gets higher. During the reaction, both species involved result in the change of oxidation state. Redox PCs occurred when ions absorbed

electrochemically onto the surface of a material with faradic charge transfer. Metal oxides such as NiO, MnO_2, Fe_3O_4, Co_3O_4, $NiCo_2O_4$, RuO_2, and conducting polymers like polypyrrole and polyaniline [21,22] are the best examples of redox pseudocapacitive materials.

(c) Intercalation Pseudocapacitance

Intercalation is the cation insertion process into the bulk lattice of the solid electrode. To maintain the electrical neutrality of the electrode, there should be an appropriate number of electrons transferred. The intercalation of pseudocapacitance is the result of the ion intercalation or the layers of redox-active materials with faradaic charge transfer without changing crystallographic structure. There is a limitation in insertion by the ability of the ion to diffuse through the electrode material.
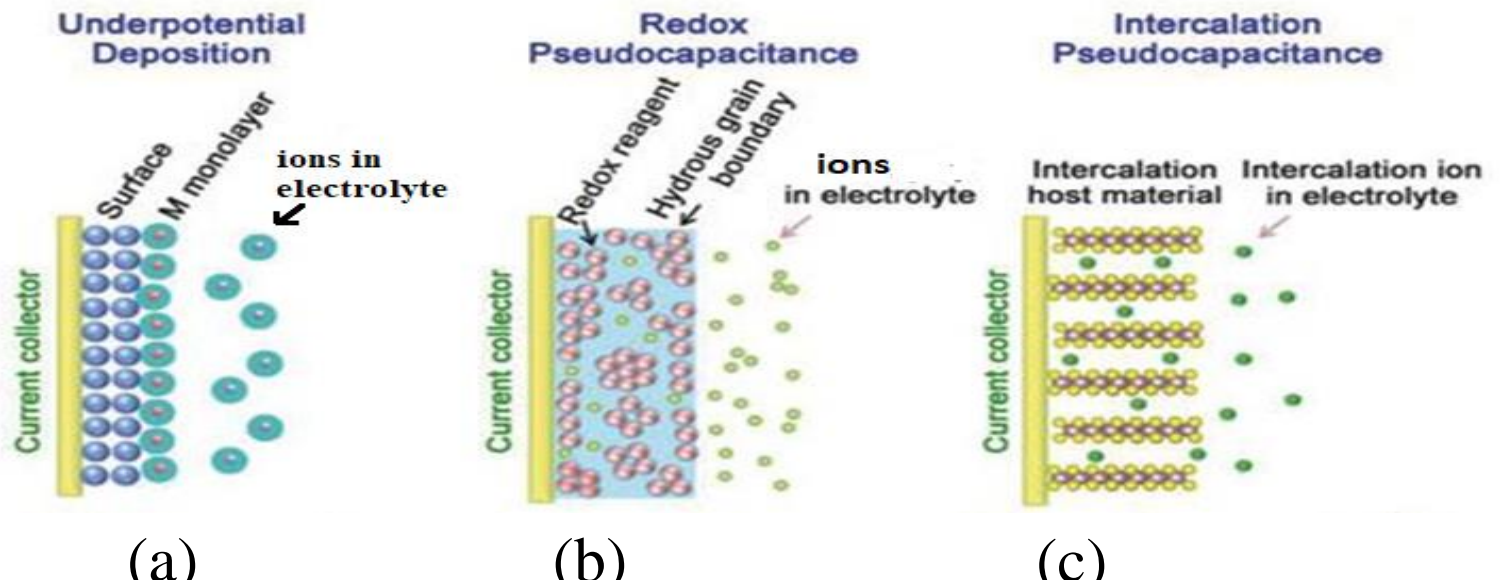
Fig.1.1.4.2.1.1 (a) underpotential deposition, (b) redox pseudocapacitance, and (c) intercalation pseudocapacitance [23]

18

1.1.4.3 Hybrid Supercapacitor

(a) Symmetric hybrid supercapacitors

In symmetric composite materials assemble in symmetrically, and materials are generally a combination of carbon material/redox material/polymer or polymer/carbon.

(b) Asymmetric hybrid supercapacitors

In the asymmetric supercapacitor electrode, the preparation method is the same as symmetric, but cell assembly is asymmetric. In these two, different composite material is assembled.

(c) Battery-type hybrid supercapacitors

Battery type hybrid supercapacitor is one of the electrodes where both carbon materials and battery type material are used. Carbon materials help to maximize the power density, and battery type help to maximize energy density.
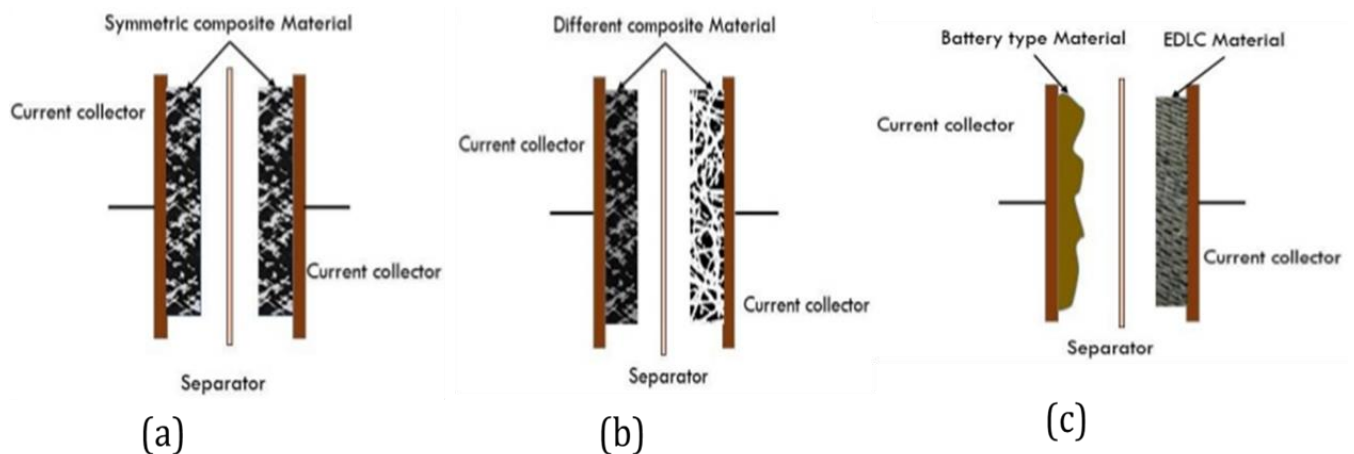
Fig. 1.1.4.3.1 (a) Symmetric hybrid supercapacitors, (b) Asymmetric hybrid supercapacitors, (c) Battery-type hybrid supercapacitors

1.2 Comparison of performance of Energy Storage Device

The Ragone plot gives a plot between power density vs. energy density of different energy storage devices like capacitors, supercapacitors, batteries, and fuel cells. Energy storage devices are classified with respect to their energy and power density, and hence Ragone chart is a standard way to visualize the energy storage performance of various devices.
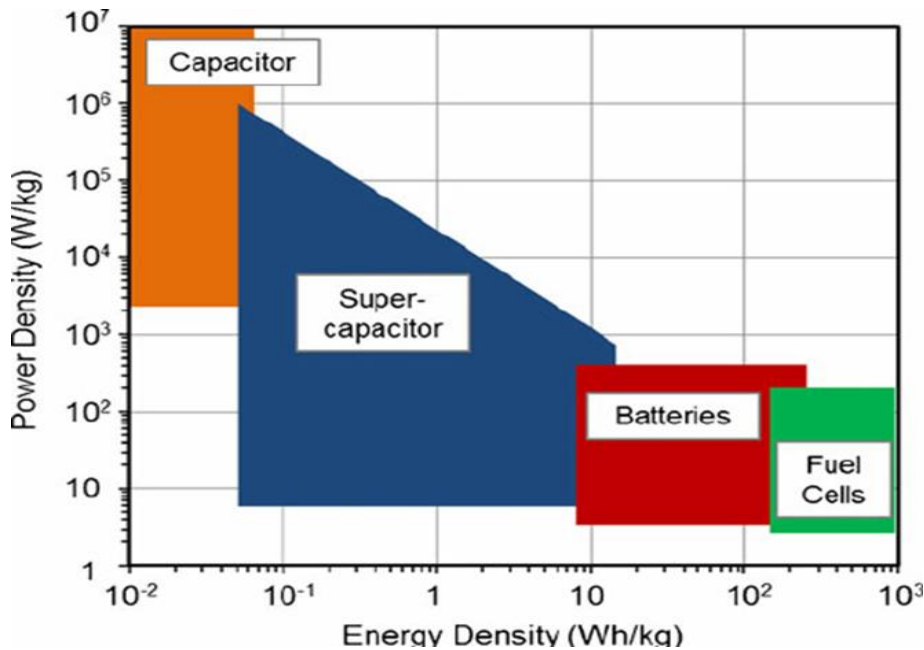
Fig. 1.2.1 Ragone plot for various energy storage device [24]

Energy density measure how much energy can store on device and power density indicate how fast the energy can be released from the system [25]. Supercapacitors can fill the gap between battery and capacitor; it acts as a bridge between them due to having more power than a battery and more energy than a capacitor. Supercapacitors can be charged or discharged very fast (only a

few seconds) with a reasonable amount of specific energy and specific power. In supercapacitors, the charging process takes place without changing any physical and chemical changes. Also, it is highly reversible and can have much longer life cycles (>100,000) and higher charging and discharge efficiency as compared to batteries or fuel cells.

1.3 Applications of pseudocapacitors

Electrochemical supercapacitors are newly emerging energy storage devices that have yet to practice in widespread applications. Currently, great advances have been made in improving characteristics like energy and power density. Novel applications for EDLCs are being discovered and promoting at an excellent rate [30]. Electrochemical supercapacitors can be highly used for commercial purposes such as on electric vehicles, battery enhancement, memory backup, improved quality of powers, smartphones, laptops, maglev trains, truck lifts, cars, power, and braking recuperation system, portable devices and so on [26].

1.4 Limitation of pseudocapacitors

The supercapacitors are highly better than batteries, capacitors, and fuel cells due to their extended lifetime, amplified rated voltage, wide range of working temperature, superior energy, and power densities, excellent cyclic stability [27]. The limitations of supercapacitors are low energy density (1/5th to1/10th of a battery), inability to use the full energy spectrum for some applications. As supercapacitors are low voltage cells, they need serial connections to get higher voltages, and also it always needs a voltage balancing element.

Also, supercapacitors are highly expensive due to the use of high-cost processes and materials. However, researchers are working to overcome this limitation of supercapacitors by working to find the cheapest materials.

1.5 Type of oxides materials

1.5.1 Ruthenium oxides (RuO_2)

Ruthenium oxides are well-known supercapacitor materials because of its high theoretical supercapacitor value ~ 2000 F/g, long life cycle life, wide potential window, high electric conductivity, high rate capability, good electrochemical reversibility. The higher value of capacitance is due to the pseudocapacitance from the surface reaction between Ru and H_+ ions. RuO_2 with water content can accelerate the diffusion of H+ ion in the electrode material. Hence, the hydrous RuO_2 exhibit high specific capacitance compared to anhydrous RuO_2 electrode. Various literature shows better performance of amorphous RuO_2 than crystalline RuO_2. Crystalline RuO_2 has limits on the insertion and extraction process, which leads to an increase in the charge transfer resistance and decrease the supercapacititve performance. On the other hand, the redox reaction of amorphous RuO_2 takes place on the surface as well as in the bulk of the electrode materials. Small-sized particles have very short diffusion and transport pathways for electrolyte ions, as well as possess a high specific surface area that provides larger electroactive sites for electrochemical reactions. Hence, instead of having many advantages, RuO_2 is not suitable for commercial applications because of its high cost, toxic nature, and scarce source.

1.5.2 Manganese oxide (MnO_2)

Manganese oxide is highly explored electrode material for the supercapacitor application due to it's higher theoretical value ~ 1360 F/g, natural abundance, environmentally friendly nature, chipper price, better chemical, and thermal stability. The crystallinity, crystal structure, morphology, conductivity, and mass loading factors affect the electrochemical properties of MnO_2. MnO_2 based electrode stored charge by pseudocapacitive mechanism. MnO_2 store electric charge due to (i) surface faradaic reaction which is due to the adsorption/desorption of electrolyte ions or proton on the surface of MnO_2 and (ii) bulk faradaic reaction which depends on the intercalation/deintercalation process of either proton or cations into the bulk of MnO_2. MnO_2 limits the bulk pseudocapacitive electrochemical reaction due to the poor electric conductivity and slower proton/cation insertion in solid. The affecting factor for supercapacitive properties is surface morphology, crystal structure, and appropriate mass loading. MnO_2 has very low electrical conductivity in the range of 10^{-4} to 10^{-6} S-1, and this results in the localized electron transfer process in a limited volume near the current collector. Hence, this leads to lower electrochemical performance, which becomes a limitation for wide use of MnO_2.

1.5.3 Nickel oxide (NiO)

Nickel oxide is one of the promising battery type electrode material for the high-performance supercapacitor device. NiO has a higher theoretical value 3750 F/g, low cost, and environmentally friendly behavior, which makes it a suitable candidate for supercapacitor application. Nanostructure NiO can provide a higher specific surface area, short diffusion pathway for an electron to perform the electrochemical reaction. Different nanostructures such as nanobelt, nanowires, nanorods, nanoplates, nanoflowers, etc. of NiO have been tested for supercapacitor applications and published in the literature. The cyclic voltammetry curve of NiO

shows oxidation/reduction peak, which corresponds to the surface oxidation and reduction. The limitation of NiO is its low electric conductivity, less cyclic stability, and operating potential which affect in electrochemical performance.

1.5.4 Cobalt oxide (Co_3O_4)

Cobalt oxide is an active electrode material with an AB_2O_4 spine structure. Co_3O_4 has higher theoretical specific capacitance∼ 3560 F/g, higher electric conductivity, and higher corrosion resistance as compared to NiO, which makes it a better supercapacitative application. Co_3O_4 is naturally abundant, environmentally safe to use, has excellent redox activity, lower cost compared to other transition metal oxides.
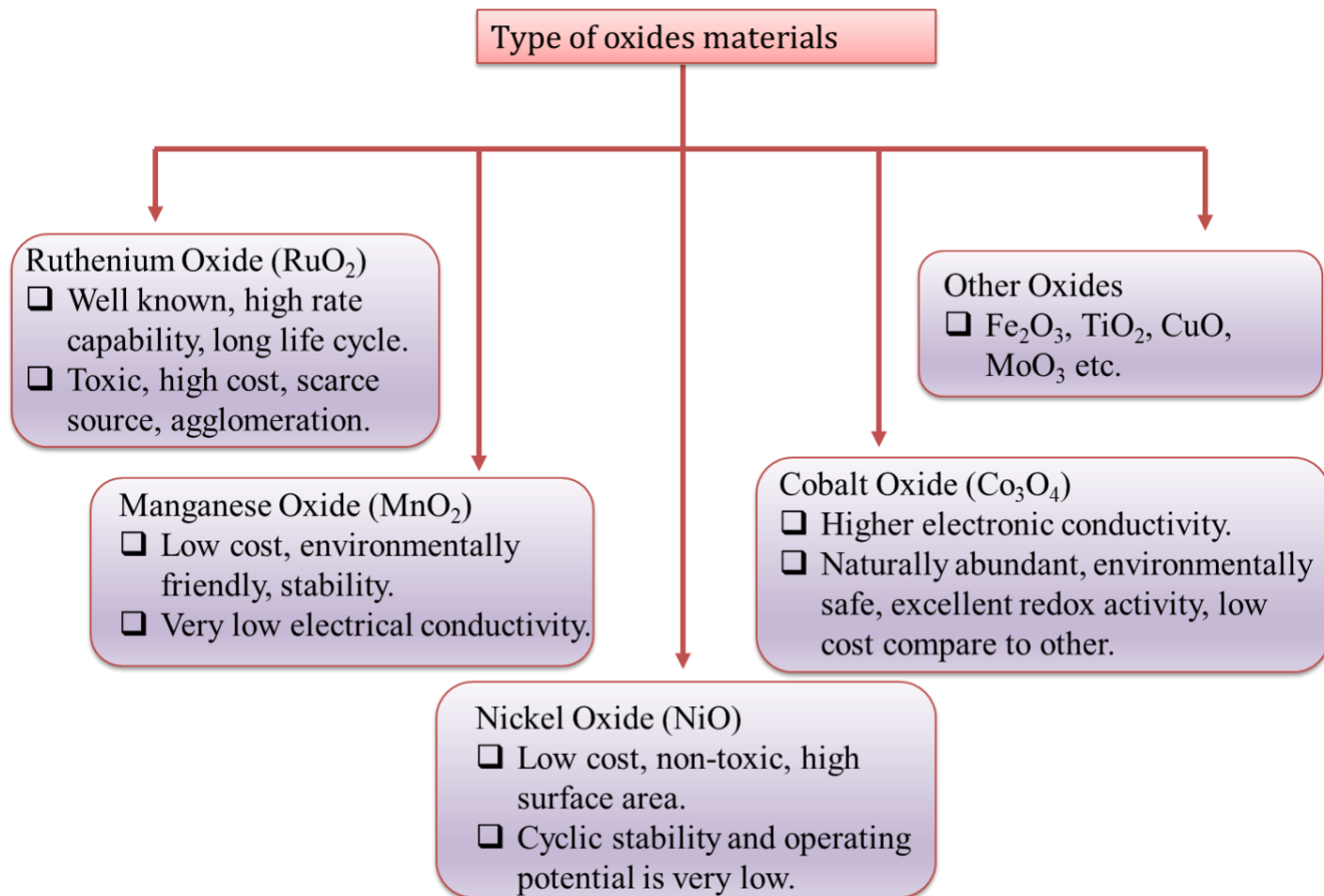
Fig. 1.5.1 Schematic for type of oxides materials.

1.6 Nanostructure synthesis routs:

Nanomaterials for the synthesis of the electrode can be prepared from different synthesis routes;

1.6.1 Hydrothermal / Solovothermal method:

Most popular procedures to prepare transition metal oxide nanostructure with controllable specific size and morphology. This process is conducted in a sealed container using a water-soluble metal precursor, and the reaction temperature is about 100 ℃. During this,

high pressure will develop and is related to reaction temperature, the percentage of the liquid-filled, and any dissolved salt. If the water is replaced by an organic solvent, the method is called solvothermal synthesis. With this method, transition metal oxide with various structures has been synthesized, such as $CuCo_2O_4$, $NiMoO_4$, Co_3O_4, $NiCo_2O_4$, etc.

1.6.2 Chemical Precipitation method:

Chemical precipitation is a facile method and suitable for large scale production of the sample. Two conditions should be satisfied when chemical precipitation occurs; first is the concentration of one solid is over the solubility limit, and second is the temperature is high enough to prompt segregation into precipitates. However, the prepared morphology is difficult to control precisely because of its fast precipitation. From this method, various morphology of supercapacitor was reported, such as $FeVO_4$ nanoparticles, $NiCo_2O_4$, etc [28,29].

1.6.3 Electrodeposition method:

This method is widely adopted to prepare nanostructured transition metal oxide. Nanostructured films with different mass loading and morphologies can be effectively and easily controlled by the careful choice of deposition solution and conductance. The process is involved with electron transfer and phase change and classified into two types; (i) anodic electrode deposition and (ii) cathodic electrodeposition based on the reaction mechanism.

1.6.4 Sol-gel method

Sol-gel method is the method in which microparticles will be agglomerated and linked together in a solution to forms a coherent network (gel) of nanostructure with high purity,

homogeneity, and porosity. This method is suitable for large scale commercial production due to its simplicity, low cost, and high yield. This sol-gel method is relatively time-consuming and complex compare to other preparation methods. Typical examples are $MnCo_2O_4$, $NiCo_2O_4$, and other transition metal oxides.

1.6.5 Microwave synthesis method

Microwave synthesis is beneficial for its higher reaction rates, shorter reaction time, better yields, and enhanced product purity due to its high penetration nature and concentrated power. Examples of these methods are preparation of $NiCo_2O_4/NiO$, including other transition metal oxides.

1.6.6 Electrospinning synthesis method

The electrospinning method is widely used for the synthesis of one-dimensional nanostructures, including nanofibers and nanotubes. The diameters of the nanostructure can be controlled by the precise management of the metal precursor concentration, the viscosity of the precursor solution, the electrospinning parameters. Examples of this method are the preparation of $ZnCo_2O_4$ nanotubes, $NiCo_2O_4$ dope carbon nanofiber@MnO_2 nanosheets, etc.

1.6.7 Other synthesis method

Many other methods are reported to prepare transition metal oxides as supercapacitor materials. Examples of other methods are a molten salt method, hot injection method, solution combustion method, micro-emulsion method, etc [30,31].

Sol-gel
- Nanoparticles agglomerate and link together in a solution to form network.

Hydrothermal/Solvothermal
- Sealed container, high pressure develop and obtain controlled size.

Chemical precipitation
- formation of separable solid substance from solution.

Electrode preparation method

Microwave
- Higher reaction rate, shorter reaction time, enhance product purity

Electrospinning
- Common method to produce nanofiber

Other synthesis
- Molten salt, hot injection, solution combustion etc.

Electrodeposition
- A process depositing solid materials on electrode surface.

Fig. 1.6.1 Schematic for nanostructure synthesis routs.

1.7 Properties of ideal electrode material

- The high specific surface area which can govern the specific capacitance.

- Controlled porosity which can affect the specific capacitance and the rate capability.

- Desirable electroactive sites, which enable pseudocapacitance.

- Higher thermal and chemical stability

- Low cost of raw material and manufacturing

- Environment friendly

CHAPTER 2

LITERATURE REVIEW

2.1 RuO_2 pseudocapacitance

Researchers have done most of the work by using mixed metal oxide materials, which shows pseudocapacitance property, and the most successful achievement was for ruthenium oxides[32]. Due to the higher cost and toxic nature of ruthenium, researchers are involved in searching for other metal oxides and nitride to use as PCs electrode. At first, ruthenium oxide for PCs was developed by Pinnacle Research Institute [33].

The first recognition of the rectangular-shaped cyclic voltammogram of a RuO_2 film was by Trasatti and Buzzanca and found it as electric double-layer capacitors. They put their effort into enhancing the capacitance as well as the fundamental understanding of the mechanism of the PCs. They found that the film of RuO_2 behaves like an electric condenser exhibiting a charging and discharging process in 1M $HClO_4$ at a scan rate of 40mV/s [34].

Bi et al. investigated RuO_2 nanoparticles on carbon nanotubes for potential electrode applications in electrochemical capacitors. Their group observed that the carbon nanotubes became a supporting material to promote the supercapacitive performance of RuO_2 and have specific capacitance as 953F/g. The result obtained from their research gives clear evidence that carbon nanotubes can improve the electrochemical performance of electrode material [35].

Hu.et.al designed an advance electrode material with a 3D, arrayed, nanotubular architecture, and annealed $RuO_2.xH_2O$ nanotubes. The property required for next-generation supercapacitor

perform by using very simple, one-step, reliable, cost-effective, anodic deposition technique. These unique structures reduce the diffusion resistance of electrolytes and enhance the facility of ion transportation and maintain the smooth electron pathway for extremely rapid charge/discharge reactions. The obtained specific power 4320 kW /kg, specific energy 7.5 W h/kg, and specific capacitance 740 F/g obtained for nanotubular arrayed $RuO_2.xH_2O$ [36].

Chen et al. develop a hybrid nanostructured electrode by RuO_2 nanowires and a single-walled carbon nanotube film. This displayed Coulombic efficiency of >99%, the specific capacitance 138 F/g, the power density of 96 kW/kg, and energy density of 18.8 Wh/kg, which indicates as promising energy storage device [37].

Liu et al. prepared a series of $Co_3O_4/RuO_2 \cdot xH_2O$ by a one-step coprecipitation method. They observed that specific capacitance and stability of composites are strongly dependent on heat treatment temperature. They prepared composite with a molar ratio of Co:Ru = 1:1, variation of temperature from 150 ºC to 900 ºC and found the highest specific capacitance of 642 F/g at 150 ºC. Capacitance gradually decreases as temperature increases, but the benefit is the recyclability of composite improved [38].

Gujar et al. deposited ruthenium oxide (RuO_2) successfully onto tin-doped indium oxide electrode and use 0.5M H_2SO_4 electrolyte. Their group found that electrochemically prepared crystalline RuO_2 remains stable for a large number of cycles and has specific capacitance 498 F/g at a scan rate of 5 mV/s. Also, they observed that the specific capacitance of the RuO_2 electrode decreases with an increase in scan rate, and hence the maximum observed capacitance was at 5 mV/s [39].

Compare to all the transition-metal oxides, ruthenium oxide is employed as the most important electrode material due to its ultrahigh pseudocapacitance and reversibility of accepting and donating protons from the aqueous electrolyte. Due to the toxicity and higher cost of Ruthenium, it is restricted for commercial applications. This limitation continuously encourages the study of suitable metal oxide for supercapacitor applications.

2.2 Supercapacitance in metal-oxides

Most of the work has been done by using ruthenium oxides, but in recent years researcher is attracted to other metal oxides due to the limitation of RuO_2. Researchers have tried to improve specific capacitance by introducing pseudo-capacitive metal oxide. Pseudocapacitance attracted more to the researcher because they can give higher specific capacitance compare to electric double layer carbonaceous materials. Metal oxides such as MnO_2, NiO, Fe_3O_4, etc. show the outstanding pseudocapacitive property, lower in cost, environmentally friendly, and practically applicable compare to RuO_2.

Zhang et al. reported a facile way to grow porous NiO nanostructures shows the different specific capacitance according to the morphology, including nanoplates, nanocolumns, and nanoslices. The different specific capacitance of NiO, such as nanocolumns (390 F/g), nanoslices (176 F/g), and nanoplates (285 F/g) at a discharge current of 5 A/g which indicate that structure and morphology depends on supercapacitative property [40].

Nam et al. prepared NiOx thin-film electrodes to use as a supercapacitor. During the study, the effect of electrodeposition condition on the surface morphology of NiO_x and found to have a significant effect on the surface morphology of the deposited film. The maximum obtained

specific capacitance 277 F/g for highly porous NiO_x film electrode, and hence it increases the surface-active sites by the formation of porous surface morphology [41].

Pang et al. deposited thin films of manganese dioxide, which was prepared by the sol-gel method on nickel foils by electrodeposition. The performance of these film as an ultracapacitor was studied by cyclic voltammetry in the range 0.0-0.9 V (SCE) which indicate better capacitive behavior with a specific capacitance of 698 F/g. Hence, the manganese dioxide thin films on nickel foils show good electrode material for the fabrication of ultracapacitor [42].

Chen et al. fabricated flexible asymmetric supercapacitors based on transition- metal-oxide nanowire/single-walled carbon nanotube hybrid thin-film electrode. These exhibit superior performance with a specific capacitance of 184 F/g, the energy density of 25.5 Wh/kg, and Columbic efficiency of 90%. Hence, electric double layer capacitance obtained from single-walled carbon nanotube and pseudocapacitance from transition metal oxide nanowires. The use of conductivity agent single-wall nanotubes results in more conductivity for the better electrochemical result [43].

Du et. al. Prepared activated carbon-Fe_3O_4 nanoparticles by microwave method and measured electrochemical properties in 6M KOH aqueous electrolyte. The supercapacitor delivered a specific capacitance of 37.9 F/g at a current density of 0.5 mA/cm_2 and 82% of initial capacity over 500 cycles. Hence the electrochemical measurement CV, EIS, and charge-discharge measurement confirm that it can be used as a hybrid supercapacitor within potential range 0 to 1.2 V [44].

Metal oxides used as active electrode materials for ECs have developed at a high rate over the past decades and may be classed as either noble or based metal oxides. However, their relatively high cost, low capacitance values, and potential (reported) harmful nature to the environment has limited their widespread application in supercapacitors.

2.3 Supercapacitance in mixed metallic oxides

A mixed transition metal oxide is designated as $A_xB_{3-x}O_4$; A, B = Co, Ni, Zn, Mn, Fe, etc., typically they have a spinel structure. Nowadays, worldwide researchers are attracted to mixed metal oxide due to their low cost, environmentally friendly nature, and so on.

Yuan et al. fabricated an advance three-dimensional mesoporous $NiCo_2O_4$ nanosheet for electrode materials. $NiCo_2O_4$ were prepared by electrodeposition of bimetallic (Ni, Co) hydroxide precursor on a Ni foam. Pseudo-capacitance performance was observed with a specific capacitance of 1450 F/g at a higher current density of 20 A/g, and excellent cyclic performance at a high rate, which indicates it as an efficient electrode for electrochemical capacitor [45].

Cheng et al. deposited $ZnCo_2O_4$ nanoflakes on nickel foam by using the hydrothermal procedure and obtained specific capacitance of 1220 F/g at a current density of 2 A/ g in a 2 M KOH aqueous solution. It shows long cyclic stability of 94.2% capacitance retention even after 5000 cycles [50]. Due to the presence of porosity $ZnCo_2O_4$, nanoflakes display large surface area, and hence it allows fast ion and electron transport improved reactivity as well as enhanced electrochemical kinetics. This is highly applicable due to the facile preparation method and cost-effective [46].

Mondal et al. synthesized the mesoporous flake like manganese cobalt oxide, i.e., MnCo2O4 by the hydrothermal method [51]. It gives a high specific capacitance of 1487 F/g at a current density of 1 A/g, and a longer cycling performance over 2000 charge/discharge cycles. This might be used as an attractive candidate for LIBs and supercapacitors [47].

Wang et al. successfully synthesized multi-shelled $CoFe_2O_4$ hollow microspheres by a one-step hydrothermal method followed by calcination at 500_0C for 2 hours and obtained multi-shelled hollow spheres. The initial capacities of the single-, double-, triple- and quadruple-shelled $CoFe_2O_4$ microspheres were 406.8, 552.8, 1,450.0, and 1,211.0 F/g, respectively. These obtained higher specific capacitance was obtained due to the unique nature and faradic pseudo-capacitance of $CoFe_2O_4$ nanoparticles [48].

After reviewing different works of literature, it is known that structure, morphology, porosity play an important role in electrochemical performance. Crystallographic nature may play an important role in improving the performance of energy storage devices such as a capacitor.

2.4 Co_3O_4 as supercapacitors

To improve supercapacitors' energy densities, numerous effort has been made to investigate pseudocapacitive transition metal oxides or hydroxide (such as RuO_2, MnO_2, NiO, Co_3O_4, $Ni(OH)_2$, $Co(OH)_2$ etc.). Their composition with conductive additive produces higher specific capacitance than typical carbonaceous materials with electric double-layer capacitance [49,50,51]. Among the available pseudo-capacitance materials, Co_3O_4 is highly attractive for supercapacitor applications due to lower cost, environmentally friendly nature, good redox activity, and higher theoretical specific capacitance ~3560 F/g [52]. However, with higher

observed theoretical value for specific capacitance, it is still challenging to improve specific capacitance, rate capability, and long-term stability with the rational design and fabrication process.

2.4.1 Crystallographic structures of Co_3O_4

Cobalt oxides (Co_3O_4) has a normal spinel crystal structure (space group $Fd\overline{3}m$) with a cubic close packing array [53]. Co_3O_4 is a magnetic p-type semiconductor and have application in sensors, heterogeneous catalysts, electronic devices, magnetic materials, supercapacitors, and solid-state sensors. It has a close-packed face-centered cubic (fcc) lattice formed by oxygen ions and cobalt ions. Cobalt ions are in two different oxidation states, Co_{2+} and Co_{3+}. They are located at the 8a interstitial tetrahedral and 16d octahedral sites.
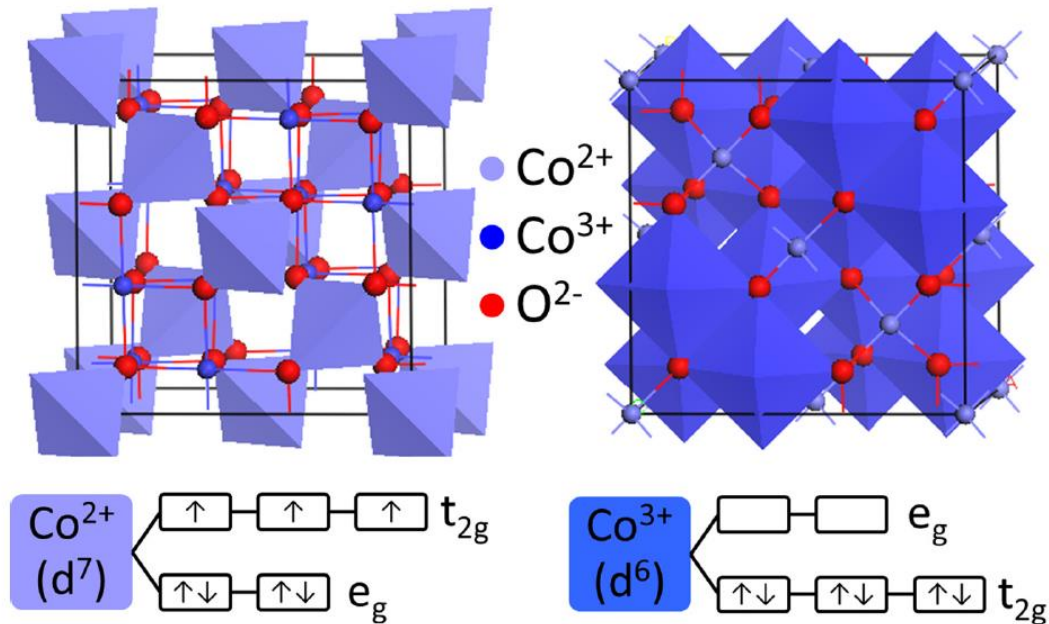
Fig.2.4.1.1 Crystallographic structure of Co_3O_4 at room temperature, Co_3O_4 assumes the normal spinel structure, based on the crystal field splitting the Co_{2p} ions (tetrahedral, light blue) carry magnetic moment, while the Co_{3p} (octahedral dark blue) ions are nonmagnetic [54].

The crystal fields at the 8a and 16d sites split the five degenerate atomic d orbitals into two groups. Where 3 unpaired d electron on Co_{2+}, on the other hand, all the d electrons of Co_{3+} are paired. Hence due to this, Co_{3+} ions are non-magnetic, whereas the Co_{2+} ions carry a magnetic moment. Experimentally, Co_3O_4 is a paramagnetic semiconductor at room temperature. It became antiferromagnetic below 40K; these anti-ferromagnetisms are mainly due to the weak coupling between nearest-neighbor Co_{2+} ions [55]. The measured values of the bandgap are around 1.6 eV, and conductivity is usually p-type at low temperature and intrinsic at high temperature.

2.5 Review of Co_3O_4 as an electrode for supercapacitors

2.5.1 Biomaterial to prepare Co_3O_4

D. Sun et al. successfully prepared Co_3O_4 by using cotton in the hydrothermal method. They annealed obtained precursor in a tubular furnace at 400 °C in air for 1, 2, and 3 h, respectively. Hence, the obtained specific capacitance (Csp) is 262.0, 284.2, and 156.8 F/g at 1 A·g−1, respectively. Hence the obtain BET specific surface area for the sample annealed at 2 hr was determined to be 67.8 m2/g, and pore volume was 0.41 cm3/g [56].

D. Yan et al. prepared Co_3O_4 by the simple and effective bio-template method. The obtained specific surface area of biomorphic Co_3O_4 is 3.0 m2/g, and for bulk Co_3O_4, it was 0.8 m2/g.

Furthermore, they measure the specific capacitances of biomorphic Co_3O_4 and bulk Co_3O_4 at 0.5 A g-1 are 130.5 F g-1 and 46.0 F/g, respectively [57].

Y. Liu et al. use Sorghum straw to synthesis tubular porous Co_3O_4 by a hydrothermal route. The obtained specific capacitance for Co_3O_4 is 107.1, 100.6, 98.7, 98.3 F/g for 0.5, 1, 2, and 3A/g, respectively. The obtained specific surface area of tubular porous Co_3O_4 was 26.5 m2/g, and the pore volume was 0.34 cm3/g [58].

Edison et al. describe a facile and green approach for the synthesis of Co_3O_4@C (carbon-supported) nanoparticles using the fruit of Terminalia chebula as a carbon precursor. They found 642 F/g specific capacitance at a current density of 1 A/g [59].

Z. Shi et al. synthesized Co_3O_4 @biomass-drived carbon fiber@ Co_3O_4 (i.e., @BCF@), composite with biomass-derived hollow carbon fiber as a sandwich layer. The measured specific capacitance was 948.9 F/g at current density 0.5 A/g [60].

S. Balasubramanian et al. synthesis of mesoporous Co_3O_4/C composites via greener route by co-precipitation method and calcined prepared samples at 400, 500, and 600 ºC. It is found that the maximum specific capacitance was 456 F/g at the scan rate of 2 mV/s of the sample, which was calcined at temperature 500 ºC. Furthermore, the maximum specific capacitance at current density 0.5 A/g was 400 F/g for this sample [61].

2.5.2 Co_3O_4 preparation by using chemicals:

Wang et.al. synthesized cobalt oxide nonporous nanorods using a facile and hydrothermal method. The higher specific capacitance of 281 F/g was obtained at a 5 mV/s scan rate in 2 M

KOH solution. The higher specific capacitance originated mainly from Faradic pseudo-capacitance, not only by electric double layer capacitance (EDLCs) [62].

J. Xu et al. synthesized Co_3O_4 nanotubes by chemically depositing cobalt hydroxide in anodic aluminum oxide. It displays good capacitive behavior with a specific capacitance of 574 F/g at a current density of 0.1A/g [63].

Cui et al. synthesized Co_3O_4 nanorods by hydrothermal method, using cetyltrimethylammonium bromide (CTAB). The obtained Co_3O_4 nanorods exhibit a specific capacitance of 456 F/g even after 500 cycles. This suggests that the potential application in electrochemical capacitors of Co3O4 is due to the maximum charge transfer process at the electrode-electrolyte interface [64].

Gao et al. prepared nanowire arrays Co_3O_4 on nickel foam via template free growth by thermal treatment at 300_0C in air. This shows maximum specific capacitance of 746 F/g measured at a current density of 5 mA/cm2 in the KOH electrolyte solution. The higher specific capacitance is due to the connection of each nanowire with nickel foam due to which all nanowire participates in the electrochemical reaction and hence utilizes active materials. Also, there are open spaces between neighboring nanowires that allow for easy diffusion of electrolyte into the inner region of the electrode and hence reduction of internal resistance [65].

2.6 Summary

In this chapter, we reviewed the recent advances in metal oxides electrode materials for supercapacitors. We found that metal oxide is the most important material to develop high-performance energy storage devices. The electrochemical performance of electrode materials is dependent on morphology and size. Transition metal oxides have a higher specific surface area,

which is responsible for providing more active sites for electrochemical reactions, short diffusion pathways for ions and electrons, effectively make difficult to change volume during the charge-discharge process for the electrochemical performance. Nanostructured electrode materials with high capacity, long life cycles, and good stability boost the performance of supercapacitors and will highly applicable. In this thesis work, a study of cobalt oxide in three different electrolytes has been done, and it is found that used electrolyte directly related to the value of specific capacitance.

CHAPTER 3

EXPERIMENTAL

The chemicals used in the preparation of nanotubular Co_3O_4 structure was cobalt nitrate hexahydrate ($Co(No_3)_2.6H_2O$), purchased from the Sigma-Aldrich company.

3.1 Sample preparation

3.1.1 Synthesis

The spinel Co_3O_4 was synthesized by a facile bio-template method. 0.59 g of cobalt nitrate hexahydrate ($Co(NO_3)_2.6H_2O$) was mixed in 10 ml of distilled water, and the mixture was ultrasonicated for 10 minutes to make a homogenous solution. 1.0 g of cotton was soaked in the cobalt nitrate solution for 5 minutes. The resulting soaked cotton was filtered and dried at 150 $_o$C for 30 minutes. The dried cotton was later calcined at 520 $_o$C for 3 hours in the air to obtain a bio-templated Co_3O_4 tubular microstructure.

$$3Co(No_3)_2.6H_2O \longrightarrow Co_3O_4 + O_2 + 6No_2 + 18\,H_2O$$
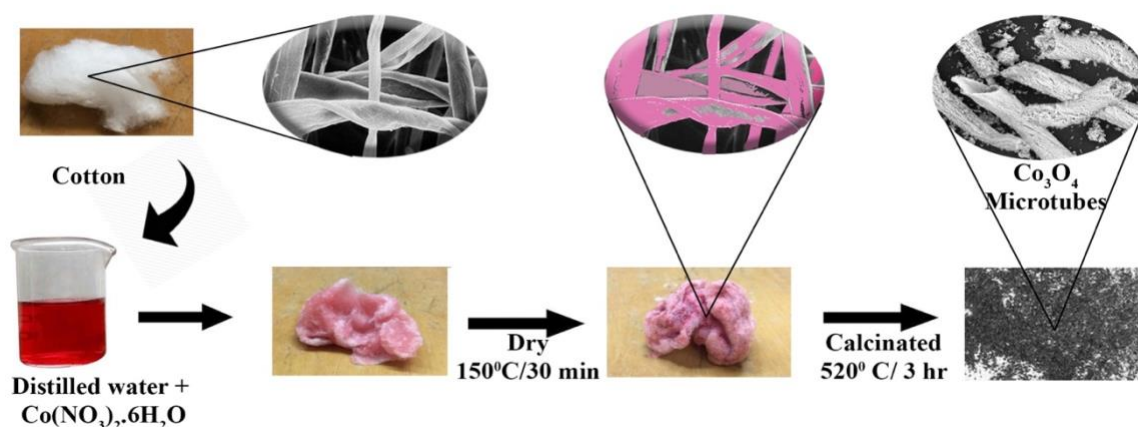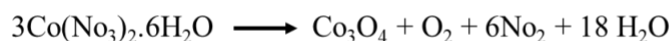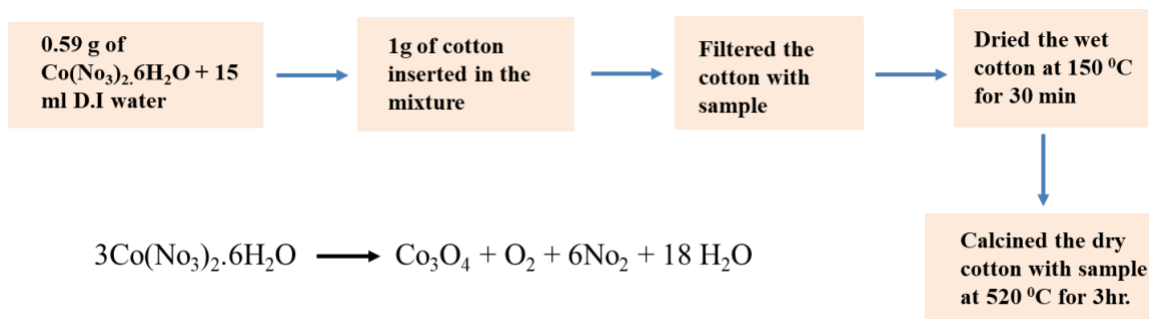
Figure 3.1.1.1 A schematic representation of the synthesis process for deriving biotempleted tubular Co₃O₄ microstructures using cotton fiber as a biotemplet. The synthesis of tubular Co₃O₄ microstructure proceeds with dipping cotton fiber is precusor solution (discussed in experimental section) followed by heat treatement. The as derived Co₃O₄ microstructure assume the form of tubular structure of cotton fiber. The final product, tubular carbon- Co₃O₄, is derived upon further calcination up to 520 ºC.

3.2 Sample characterization

3.2.1. X-ray diffraction (XRD)

X-ray diffraction is a device used to the characterization of the crystal phase, its structure, and the property of crystalline materials. The components such as atoms, ions, and molecules in crystalline materials arranged in a regular pattern. XRD generates an x-ray beam hitting a sample as a function of incident and scattered angle. The scattered X-rays from the sample interfere with each other either by constructively or destructively. The detector can read signals only at angles where constructive interference occurs. All the samples have a particular arrangement within their unit cell. Hence, as x-ray hits on the sample, it leads to a relative intensity of the recorded diffraction peak. As a result of this, the angular positions of the x-ray diffraction resolved the size and geometry of unit cells. The resultant diffraction lines with peaks together are called x-ray diffraction patterns. The wavelength of the x-ray is comparable to the atomic size because this x-ray is suitable for examining the structural arrangement of atoms and molecules in a wide range of materials. Each crystal has its own unique characteristics x-ray diffraction pattern based on Bragg's law:

$$n\lambda = 2d \sin \theta$$
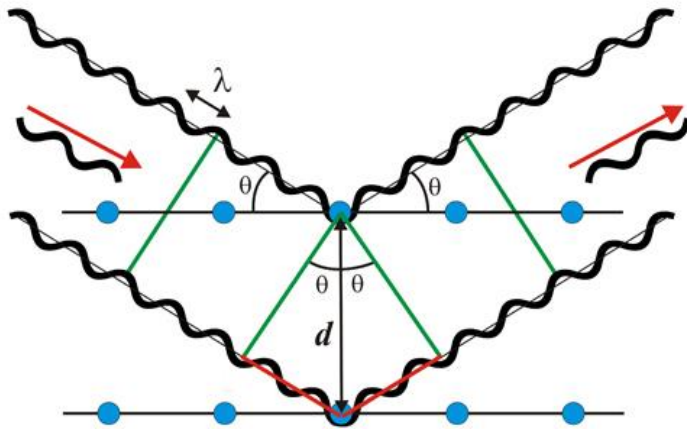
Figure 3.2.1.1: Schematic of X-ray powder diffraction [66].

Where n is an integer called the order of reflection, λ is the wavelength of the x-rays, d is the characteristic spacing between the crystal planes of specimen called interplanar spacing. Interplanar spacing d can be determined by measuring the angles θ, under which the constructively interfering x-ray leaves the crystal.

In this research work, we have used XRD to determine the actual phase of the material by comparing the obtained XRD pattern to the known standard diffraction lines in the International Centre for Diffraction Data (ICDD) database. Prepared samples were mounted on a zero background sample holder. The XRD test is non-destructive; hence the material can be reused for other tests. Structural characterization including phase purity, lattice parameter, crystalline size, lattice strain was performed on powder samples using x-ray diffractometer (D8 Advance Bruker Inc.) with Cu-Kα radiation (λ=1.54056 Å).

3.2.2 Scanning electron microscopy (SEM)

The scanning electron microscope (SEM) is a type of electron microscope that uses electrons instead of light to form an image. SEM can give much more control on degree of magnification to examine the details within nanostructure due to use of electromagnets instead of lenses. The excited beam of an electron is produced at the top of the microscope by an electron gun due to the heating of metal filament. The electron beam makes its vertical way through electromagnetic

lenses, which focus the beam down towards the sample and scan the sample in a raster scan pattern with the exciting beam of electrons. As the beam hits the sample, it emits secondary electrons from the sample, and this number of detected electrons depends on the variations of the surface of the sample. Scanning of the surface by the beam, detecting the variation of a number of electrons, collecting the X-rays (produced by the ionization of surface atom by electrons), backscattered electrons, and secondary electrons containing information of surface morphology and converted them into a signal that sent to the screen. In this work, SEM was employed to characterize the morphology and surface structure of prepared electrode materials. The SEM specimens can be prepared by spreading sample powder directly onto the carbon tape and then air-drying. All the measurements were carried out by using Phenom, SEM, at 10 keV.

3.2.3 Brunauer-Emmett-Teller (BET) nitrogen adsorption-desorption isotherms

Brunauer-Emmett-Teller (BET) and Barrett-Joyner-Halenda (BJH) method are used to determine surface area, pore size, and pore volume of the desired materials. BET analysis examines the external area and pore area of the materials to determine the total specific surface area in m_2/g by nitrogen multilayer adsorption isotherms. Sample containing moisture and other contaminants must be removed. Hence, the sample evacuated or purged with inert gas by heating to deserve the moisture and other volatile species to avoid interference in the analysis. The first sample is evacuated and cool to the temperature of 77K, i.e., the temperature of liquid nitrogen. The actual measurement of the sample begins with low pressure of adsorption gas, and the pressure of gas rises and hence the amount of adsorbed at the surface until the monolayer formed. This used to calculate BET. BJH analysis can also be employed to determine the pore area and specific pore volume using nitrogen adsorption and desorption techniques to characterize the pore size

distribution of the sample. All the surface area measurements were carried out using Autosorb-1, (Quanta chrome, Boynton Beach, FL 33426, model no. AS1MP) using nitrogen as adsorbing gas at 77 K.

3.2.4. Fourier transform infrared spectroscopy (FTIR):

Fourier Transform Infrared Spectroscopy (FTIR) is a technique used to obtain an infrared spectrum of absorption of a solid, liquid or gas sample. When infrared radiation passed through the sample, the wave, which is equal to the energy of the molecule it gets absorbed and the wave which is not equal to the energy of the molecule it gets to transmit. The transmitted IR light detected by the detector, which creates molecular fingerprint (no two unique molecules produce the same infrared spectrum). Hence, there obtained an energy vs. time curve, which is automatically converted in the Energy vs. frequency curve by using Fourier transform relation. FTIR can identify unknown materials, quality, consistency, amount of component in a mixture, functional group, and structure of the sample. Fourier transforms infrared (FTIR) spectra were recorded on a Thermo Scientific (Nicolet iS10) between 350 and 1200 cm$_{-1}$.

3.2.5. Thermogravimetry analysis (TGA):

Thermogravimetric analysis (TGA) measures weight changes in a material as a function of temperature (or time) under a controlled atmosphere. The measured weight loss curves give information on changes in sample composition, thermal stability, and kinetic parameters for a chemical reaction in the sample. This weight loss may be due to gas obtained by decomposition of reactants heating. Also, the loss may be due to water of crystallization or water of constituent.

TGA can analyze only the solid substance and plotted a graph of mass vs. temperature (or time), which is called a thermogram. Thermogram is the characteristic curve for a given material. TGA was performed in the temperature range of 24 to 550 $_o$C using TGA (Instrument Specialist, Inc.)

3.3 Fabrication of the electrodes and electrochemical testing

3.3.1 Electrode Fabrication Procedure

The working electrode was prepared by mixing 80 wt.% of the synthesized powder, 10 wt.% of acetylene black, and 10 wt.% of polyvinylidene difluoride (PVDF) in the presence of N-methyl pyrrolidinone (NMP). After mixing the components, the slurry was pasted onto nickel foam. The prepared electrode was dried at 60 °C under vacuum for 10 hours. The loading mass of all samples on nickel foam was about 2-3 mg. The deposited weight was measured by weighing the nickel foam before and after deposition with an analytical balance (model MS105DU, Mettler Toledo, max. 120 g, 0.01 mg of resolution). A platinum wire as a counter electrode, a saturated calomel electrode (SCE) as a reference electrode, and cobalt oxides on nickel foam as a working electrode was used. The electrochemical performance of the Co_3O_4 electrode was evaluated in 3 M KOH, NaOH, or LiOH was used as an electrolyte.

3.3.2 Electrochemical measurement:

In electrochemical experiments, an electrochemical reaction occurs in a sample and solution inside a cell, and the electrical response is measured. In general electrochemical measurements, and electrodes are immersed in a test solution (electrolyte).

3.3.3 Electrode

The electrode is the surface where oxidation or reduction half-reaction occurs. There are mainly two types of electrode system;

3.3.3.1 Two electrode system

In two electrodes system, after applying a known current or by potential between working and counter electrodes can measure other variables. In the two-electrode counter electrode function as cathode and working electrode perform like anode. Potential of counter electrode change during the measurement like reference electrode, but in reality, there is no reference electrode. Hence efficiency is by working and counter electrodes.

3.3.3.2 Three electrode system

In a three-electrode system, it has three electrodes; counter, working, and reference. The counter electrode, along with the working electrode, provides a circuit over which current is applied or measured. The potential of the counter electrode is adjusted to balance the reaction occurring at the working electrode.

(a) The counter electrode (CE): The counter electrode (auxiliary electrode) closes the current circuit in the electrochemical cell. It does not participate in the electrochemical reaction, but it helps to pass a current. Examples of CE are Pt, Au, graphite, glassy carbon, etc. Current flow in between WE and CE, the total surface area of CE should be higher than the area of WE so that it will not be a limiting factor in the kinetics of the electrochemical process. Hence, the counter electrode has to be able to transfer electrons quickly in order to prevent any inhibition of electron transfer at the working electrode.

(b) The working electrode (WE): In a three-electrode system, the current flows between the CE and the WE. The potential difference is controlled between the WE and CE, and it is measured between the RE and WE, where RE should keep close to WE. WE are held at fixed and stable potential by controlling the polarization of the CE, and the potential difference between RE and WE is controlled all the time. The potential difference between the WE and CE usually is not to measure; it is adjusted so that the potential difference between the WE and RE will be equal to the potential difference specified by the user. The working electrode is called cathode or anode, depending on whether the reaction on the electrode is reduction or oxidation.

(c) The reference electrode (RE): The reference electrode is an electrode which has a stable and well-known electrode potential. High stability of the electrode potential is usually reached by employing a redox system with a constant concentration of each participant of the redox reaction. Its function is to find the electrode potential of the unknown electrode. RE is of two types; Primary RE and Secondary RE. The RE whose potential is taken as zero is called a primary reference electrode. The standard Hydrogen electrode is an example of the primary electrode. The RE whose potential is exactly known and the electrode potential value is depends on the concentration of the solution in which it is dipped. The calomel electrode is an example of a second electrode. Hence, the reference electrode is the electrode to which the potential of the working electrode is referenced.
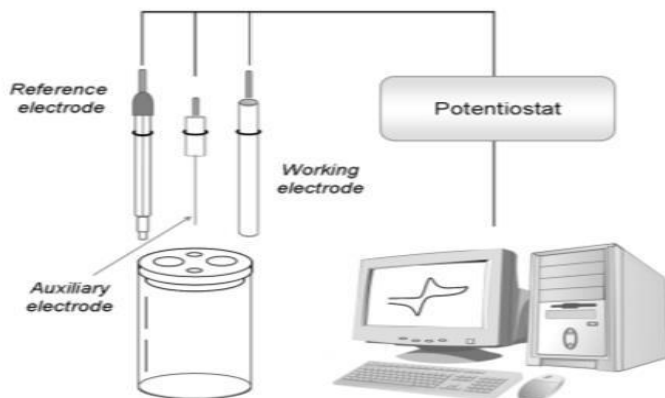
Fig 3.3.3.2.1 is the schematic representation of the three-electrode cell. It comprises of working electrode, a counter electrode (platinum rod), and the reference electrode (saturated calomel electrode, SCE) assembled in a cell dipped inside aqueous electrolyte. The electrodes were dipped in the electrolyte a few hours before the experiment is operated, to get electrolyte fully penetrated into the working electrode.

3.3.4 Electrolyte

The substance which produces an electrically conducting solution when dissolved in a polar solvent is called an electrolyte. The dissolved electrolyte separates into cations and anions which disperse uniformly through the solvent. When electric potential applied to such a solution, the cations of solution drive towards the electrode, which have an abundance of electrons, on the other hand, anions are drive to the electrode that has a deficiency of electron. To improve the performance of SCs, various types of electrolytes have been reported in the literature. Possible characterization of electrolytes for metal oxide SCs ate liquid, redox additive, and solid or gel state.

3.3.5 Cell assembly

For the supercapacitor test, the beaker-type three-electrode cell was assembled with a working electrode, a counter electrode (platinum foil), and a reference electrode (saturated calomel electrode, SCE) which place close to working electrode. **Fig.3.3.3.2.1** shows the schematic representation of the electrochemical cell. In this study 3M KOH was used as an electrolyte. Before electrochemical testing, the three-electrode cell was left for one or two hours so that electrolyte solution can penetrate into the working electrode.

3.3.6 Electrochemical Testing

Electrochemistry is a branch of chemistry that studies chemical reactions that take place in a solution at the interface of an electron conductor and an ionic conductor, and which involve electron transfer between the electrode and the electrolyte or species in solution. In this study, the electrochemical properties were evaluated by cyclic voltammetry, galvanostatic charge-discharge, and electrochemical Impedance Spectroscopy which are discussed below;

3.3.6.1 Cyclic voltammetry (CV)

Cyclic voltammetry (CV) is an important tool to study electrochemical reactions (oxidation and reduction) and the electrochemical reversibility. It is a type of potentiodynamic measurement that can be used to record a relationship of current vs. voltage. The measurement is taken when the potential at the working electrode is ramped linearly versus time (at a particular scan rate) to a set potential and reversed back to the original potential at the same scan rate.

For lithium-ion batteries and supercapacitors, an ideal CV curve for a reversible reaction consists of two peaks opposite each other, as one process is anodic and the other is cathodic, and further confirm the energy storage mechanism involved. In this thesis, CV was conducted using a standard three-electrode system on a Versa STAT 4-500 electrochemical workstation (Princeton Applied Research, USA) at different scan rates and voltage ranges at room temperature. The electrochemical characterization of the as-prepared electrode was carried out using a standard three-electrode system, as discussed above. Cyclic voltammetry (CV) and galvanostatic charge-discharge were tested within a potential range of 0.0 to 0.6 V. CV is an important tool to study the oxidation and reduction reaction and the electrochemical reversibility of the materials where the relationship between current and voltage is established. Voltammetry curves were obtained at different scan rates of 2, 5, 10, 20, 30, 50, 75, 100, 125, 150, 175, 200, 225 and 250 mV/s. The total specific capacitance, C_{sp} of the materials, was calculated from the CV curves based on the following equation [19].

$$C_{sp} = \frac{\int_{V_1}^{V_2} i \times V \times dv}{m \times v \times (V_2 - V_1)} \quad \ldots\ldots\ldots\ldots\ldots..(3.3.6.1.1\ )$$

3.3.6.2 Galvanostatic charge-discharge (GCD)

For the three-electrode supercapacitors test system, the galvanostatic charge-discharge performance is examined by a chronopotentiometry technique on an electrochemistry workstation with an aqueous electrolyte. The rate capability and specific capacitance of the Co_3O_4 electrodes were performed using charge/discharge measurements. In the galvanostatic

charge-discharge experiments, a potential vs. time response is recorded at the constant current density, and we have tested the charge-discharge measurement at a different constant current density of 0.5, 0.75, 1, 1.5, 2, 3, 4, 5 and 7 A/g for every sample. It is commonly used to measure the specific capacity, cycling performance, and the Coulombic efficiency of the working electrodes. The charge storage capacity from the galvanostatic charge-discharge measurements was calculated using the following equation [67]:

$$C_{sp} = \frac{I \times t}{m \times \Delta V} \quad \text{................ (3.3.6.2.1)}$$

Where I (A) is current, (ΔV) is the width of the potential window and mass 'm' of the active material loaded on the electrode, and 'u' is the scan rate.

3.3.6.3 Electrochemical Impedance Spectroscopy (EIS):

Electrochemical Impedance Spectroscopy (EIS) was also tested to evaluate materials capacitive performance in the frequency domain region. The variation of the resistance with the frequency can be measured by monitoring the current response. This provides an estimation of the internal resistance with an open circuit potential under several other conditions.

CHAPTER 4

RESULT AND DISCUSSION

The phase purity and crystalline parameters of the samples were assessed using the x-ray diffraction (XRD) pattern. The morphology of the samples was analyzed using a scanning electron microscope (Phenom) at 10 keV. The specific surface area of the samples was measured using the Brunauer-Emmett-Teller (BET) method. The thermogravimetric analyses curve and Fourier transform infrared (FTIR) spectra were recorded. The electrochemical performance of the Co_3O_4 electrode was evaluated in 3 M KOH, NaOH, or LiOH was used as an electrolyte. The electrochemical performance of the electrodes was evaluated by cyclic voltammetry (CV) and galvanostatic charge-discharge techniques (GCD). Electrochemical impedance spectroscopy (EIS) measurements were performed as a function of frequency at room temperature.

Figure 4.1(a) displays the XRD patterns of the bio-templated Co_3O_4 microstructure. The XRD patterns match with the face-centered cubic phase of Co_3O_4. The lattice constants obtained using d-spacing for the sample is $a=b=c=0.8065$ nm consistent with the standard values of cubic Co_3O_4 ($a=b=c=0.8083$ nm). The crystallite size of Co_3O_4, calculated using Scherrer's formula [68] was around 35.84 nm. FT-IR spectrum Figure 4.1(b) further identifies the structure of the bio-templated Co_3O_4. The IR spectrum displays two distinct and sharp bands at 552 (v_1) and 655 (v_2) cm^{-1}, which originate from the stretching vibrations of the metal-oxygen bond [69,70,71]. The v_1 band is characteristic of OCo_3 vibrations (Co_{3+} in octahedral coordination), and the v_2 band is attributable to $Co_{2+}Co_{3+}O_3$ (Co_{2+} in tetrahedral coordination) vibrations in the spinel lattice [72]. The presence of these bands confirms the formation of phase-pure Co_3O_4 nanostructure.

The BET, specific surface area of tubular Co_3O_4 microstructure, was determined by N_2 adsorption-desorption isotherms at 77 K between relative pressure $P/P_o \sim 0.029$ to 0.99, and the corresponding pore size distributions are calculated by Barrette-Joyner-Halenda (BJH) method, as displayed in Figure 4.1(c). The isotherm shape exhibits the type IV isotherm hysteresis loop [73], suggesting the presence of mesopores in the product. The specific surface area of biomorphic Co_3O_4 is 20.63 m_2/g, much larger than that of bulk Co_3O_4 (0.8 m_2/g) and cotton templated Co_3O_4 (3 m_2/g) [74]. From the curves, it can be observed that the largest number of pores were distributed at around 0.8 nm with the highest pore volume and should be more favorable for rapid ion transport within the electrode surface. Considering the diameter of solvated ions $\sim$ 30 Å [75,76], the best electrode materials for electrical double-layer capacitors are those who use mesoporous electrode materials with an open pore size of $\sim$ 2.0–6.0 nm [77,78,79]. It is expected that large BET surface area of tabular Co_3O_4 superstructures, can provide plenty of superficial electrochemical active sites to participate in the Faradaic redox reactions. Furthermore, appropriate pore size distribution, between 0.5-3.2 nm, as observed for template Co_3O_4, inset Figure 4.1(c), can offer additional efficient transport pathway for electrolyte molecules to their interior voids during the charge/discharge storage process and give rise to the excellent electrochemical property to the electrode material, which is critical for the electrochemical performance [10,80,81].

The thermogravimetric analysis was performed on the infiltrated sample to trace the formation of biomorphic Co_3O_4 as a function of temperature, Figure 4.1(d). The formation of Co_3O_4 from the nitrate salts results in three steps. The weight loss at around 110 $_oC$ is due to water desorption, the second weight loss of 32% up to 241 $_oC$ is due to burning of cotton and start of decomposition of $Co(NO_3)_2.6H_2O$, and no weight loss at beyond 323 $_oC$ signifies the

formation of Co_3O_4 is completed. Upon immersing fiber into the precursor solution, the water and Co $(NO_3)_2$ molecules were absorbed onto the hydroxyl-group-rich cotton fiber substrate. With the heat treatment above 520 $_oC$, $Co(NO_3)_2 \cdot 6H_2O$ dissociates to form Co_3O_4 as follow [82],

$$3Co(NO_3)_2 .6H_2O \rightarrow Co_3O_4 + O_2 + 6NO_2 + 18H_2O \text{ ... (4.1)}$$
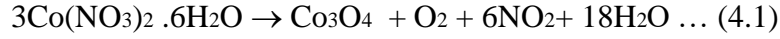
With the further increase in the calcination temperature, the precise reproduction of cotton texture was achieved after the complete removal of the organic substance.
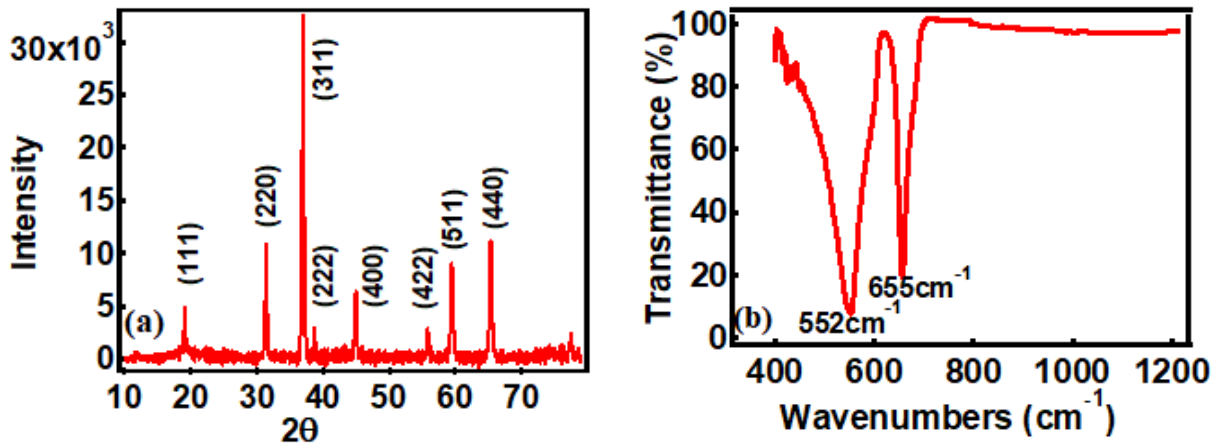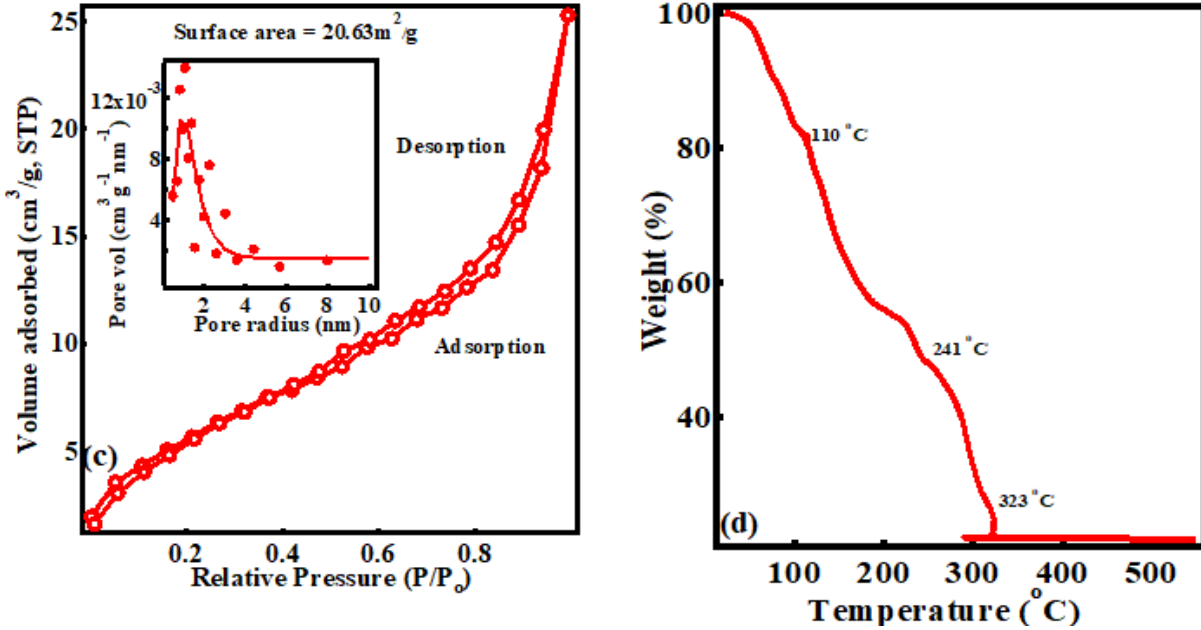
Figure 4.1 (a) X-ray diffraction pattern, (b) FTIR, (c) adsorption-desorption curve and inset pore volume distribution, and (d) thermogravimetric curve of tubular Co_3O_4 structure.

The morphologies of the as-prepared samples are examined by FE-SEM, as shown in Figure 3. SEM images display that the samples have a tubular morphology Figure 4.2(b), which resembles that of cotton Figure 4.2(a). The as-prepared Co_3O_4 inherits the morphology of cotton and exhibits a biomorphic structure. SEM images obtained using elemental mapping at cobalt peak show that the tubular structure is well decorated with the Co_3O_4 nanoparticles, Figure 4.2(d). The Co_3O_4 decorated tubular microstructure has an average outer diameter of 9.02 μm and the inner diameter of 6.15 μm, with an average thickness of 2.87 μm. Based on the above thermal results and observed morphology, a scheme for the synthesis of biotemplated Co_3O_4 tubular microstructure is proposed, as shown in Figure 4.2.
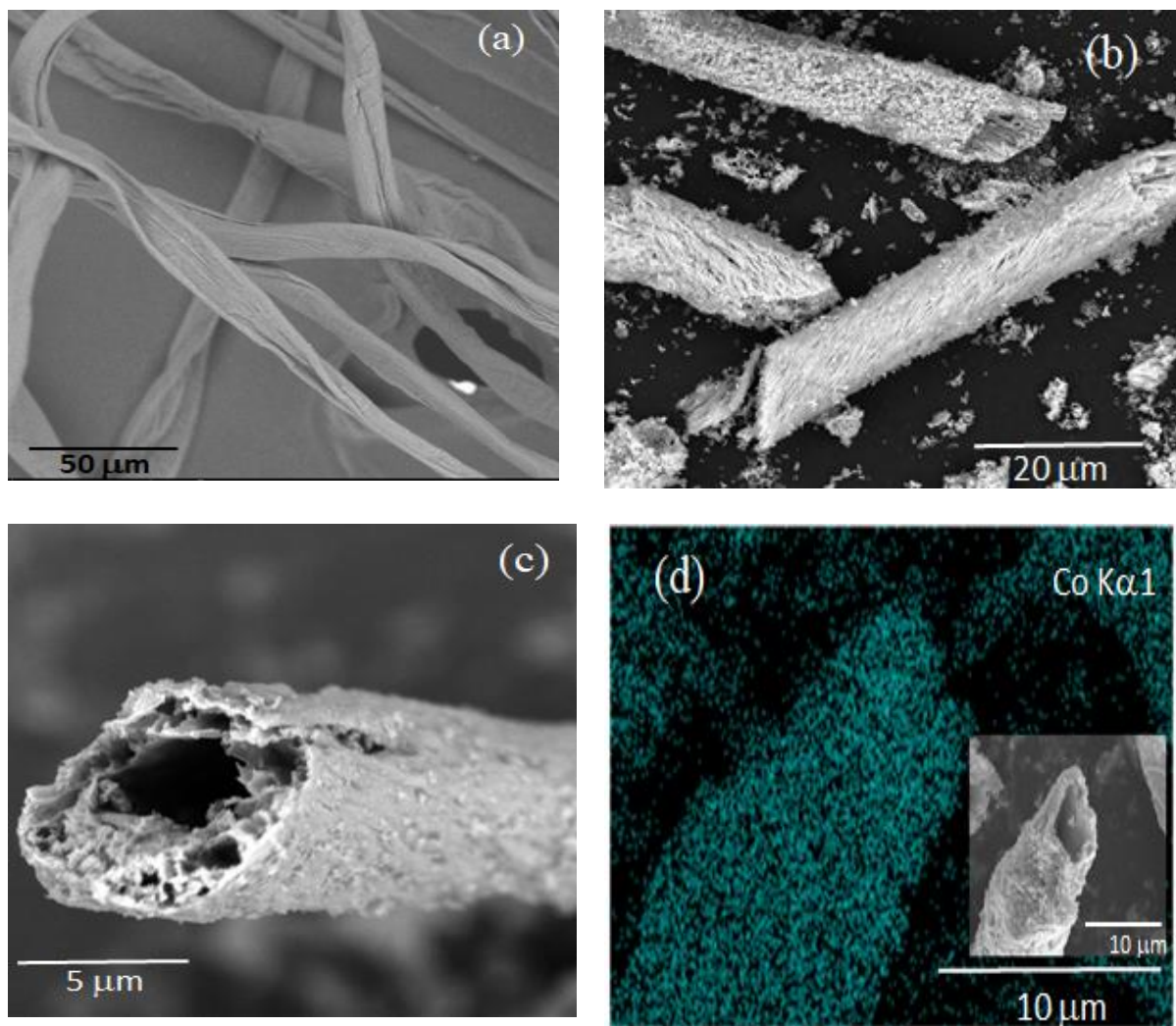
Figure 4.2 SEM images of (a) cotton fiber, (b) and (c) bio-templated tubular Co_3O_4 structure, (d) high magnification and EDX map of tubular Co_3O_4 structure.

Besides morphological parameters, the type of electrolytes and their molar concentration play an important role in determining the electrochemical behavior of oxide electrodes

[83,84,85]. Therefore, many aqueous electrolytes such as H_2SO_4, KOH, K_2SO_4, KCl, KNO_3, NaOH, Na_2SO_4, NaCl, LiOH, Li_2SO_4, etc. have been explored as electrolytes in supercapacitors [86,87,88,89,90]. In fact, the choice of an ideal electrolyte depends on the electrode material properties and intercalation efficiency of the cations, which ultimately lead to the resulting performance of supercapacitor devices [43]. The electrochemical performances of Co_3O_4 nanostructures as electrode materials for pseudocapacitors were evaluated by cyclic voltammetry measurement and galvanostatic charge/discharge in three different electrolytes viz. 3 M KOH, NaOH, and LiOH.

Cyclic voltammetry (CV) and charge-discharge curves were measured to investigate the electrochemical behavior of Co_3O_4 nanoparticles. Figure 4.3 summarizes the CV results for tubular Co_3O_4 electrodes measured in three different electrolytes, viz. 3M KOH, NaOH, and LiOH. The CV curves were measured in the voltage window of 0.0 to 0.6V and were obtained at different scan rates from 2 to 300 mV/s. All the CV plots exhibit a pair of redox peaks associated with the redox reactions involved in the alkaline electrolyte during the charging and discharging process. The capacitance characteristic of the Co_3O_4 nanostructures is that of typical pseudo-capacitance arising from the reversible surface or near-surface Faradic reactions for charge storage. The detailed electrochemical process of the Co_3O_4 nanostructures is illustrated by cyclic voltammograms (CVs). The redox reactions involved during the charge and discharge process, for Co_3O_4, can be described as follows, eq. (ii) and (iii) [91]. Two typical redox couples are noticed in the CV curve. The first redox couple was attributed to the conversion between Co_3O_4 and CoOOH, expressed as follows:

Co_3O_4 + OH^- + H_2O $\leftrightarrow$ 3CoOOH + e^- … (4.2)
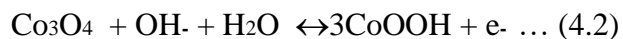
The second redox couple corresponds to the reversible reaction between CoOOH and CoO_2, represented by the following reaction:

$CoOOH + OH^- \leftrightarrow CoO_2 + H_2O + e^-$ … (4.3)

A non-rectangular form of CV curves is indicative of the pseudocapacitive characteristics of electrodes. A pair of reversible redox peaks can be observed within the potential range from 0.0 to 0.6 V. The anodic peak is due to the oxidation of Co_3O_4 to CoO_2 while the cathodic peak is for the reverse process. A small positive shift of the oxidation peak potential and a negative shift of the reduction peak potential have been observed with an increased scan rate, which can be primarily attributed to the influence of the increasing electrochemical polarization as the scan rate scales up. Pairs of reversible redox curve are indicating pseudocapacitance behavior of the material with redox peaks attributed M(II)/M(III) redox couples [92]. The shape and redox potentials of the CV curves are comparable to those reported for cobaltite [93], suggesting that the measured capacitance is mainly due to the redox mechanism.

Figure 4.3 (g) shows the specific capacitance of the tubular Co_3O_4 electrode as a function of the voltage scan rate. The specific capacitance was calculated from the CV plot using the following equation [94].

$$C_{sp} = \frac{\int_{V_1}^{V_2} i \times V \times dv}{m \times v \times (V_2 - V_1)} \qquad …(4.4) \qquad\qquad (10)$$

Where V_1 and V_2 are the limits of the working potential, i is the corresponding current, m is the mass of the electroactive materials, and v is the scan rate in mV/s.

It is evident from the figure that the electrode display higher specific capacitance up to 828 F/g in KOH electrolyte at 2 mV/s, which is ~ 40% higher than the value that is observed for either NaOH (Csp ~ 370 F/g) or LiOH (Csp ~ 319 F/g) electrolyte. The specific capacitance is rather better than the capacitance of other reported cobalt oxides, which is ranging from 110 F/g for powders prepared by hydrothermal synthesis [95] to 570 F/g for nanorods synthesized by chemical deposition [96]. The specific capacitance remained practically constant for higher scan rates (>50 mV/s) primarily because the ion movement is limited only to the surfaces of the electrode material at such conditions. The EDLC is the dominant mechanism at higher scan rates. The majority of active surfaces are utilized by the ions for charge storage at the lower scan rates (< 5 mV/s), thereby resulting in the higher specific capacitance. The CV cyclic stability of the electrode was tested for 1,000 cycles, Figure 4.4(d)-(f), which shows some noticeable differences in the CV curves dependence using different electrolytes, a difference likely arising from the difference in the charge stored during the redox reaction [97].

It is clear from the CV curves that the current response shows a proportional increase with the scan rate, indicating the good capacitive behavior of the electrode materials, which in turn can be ascribed to facile ion diffusion and large specific surface area of the electrode materials. Moreover, the shape of the CV curves is nearly independent of the scan rates, which can be attributed to the improved mass transportation and electron conduction of the electrode material [98].

The total stored charge has a contribution from three components viz. (1) the Faradaic contribution from the positive electrolyte ions insertion process, (2) the faradaic contribution from the charge-transfer process with surface atoms, and (3) referred to as pseudocapacitance and the nonfaradaic contribution from the double layer effect. Due to the high surface area of nanoparticles, both types of capacitive effects, pseudocapacitance, and double-layer charging can be substantial. These capacitive effects were characterized by analyzing the cyclic voltammetry data at various scan rates according to [99,100]

$$i = aV^b \quad \dots (4.5)$$

Where i is the peak current (A), V is the scan rate (mV/s), and a and b are fitting parameters. The charge storage mechanism is defined based on the value of the constant b, where $b = 1$ defines capacitive or $b = 0.5$ defines diffusion-limited charge storage mechanism. Fitting the peak current vs. square root of the scan rate curve, Figure 4.3 (h), with eq. (v) gives b values of ~ 0.67, 0.58, 0.63 for KOH, NaOH, and LiOH electrolytes, respectively. This indicates that the charge storage mechanism is more capacitive with KOH electrolytes as compared to the other two.

Usually, the current response at a fixed potential as being the combination of two separate mechanisms, surface capacitive effects, and diffusion-controlled insertion processes [101,102], these contributions could be separated using the following equation:

$$C_{sp} = k_1 + k_2 v^{-1/2} \dots (4.6)$$

For which k_1 and k_2 can be determined from the C vs.$v_{-1/2}$ linear plot with slope k_2 and intercept k_1. k_1 and k_2 are fractions of diffusion and capacitive contribution to the net specific capacitance at a given voltage rate. The specific capacitance was plotted against the slow scan rate up to 20 mV/s, and a regression fit was performed using Eq. (vi). The obtained k_1 and k_2 values were used

to determine the fractional contribution to the net specific capacitance. Figure 4.3 (i) shows capacitive and diffusive fractional contributions to net specific capacitance for a slow scan rate of up to 20 mV/s. By comparing the unshaded area with the total capacitance, we find that capacitive effects contribute by 78, 58, 56% of the total specific capacitance for KOH, NaOH, and LiOH, respectively.
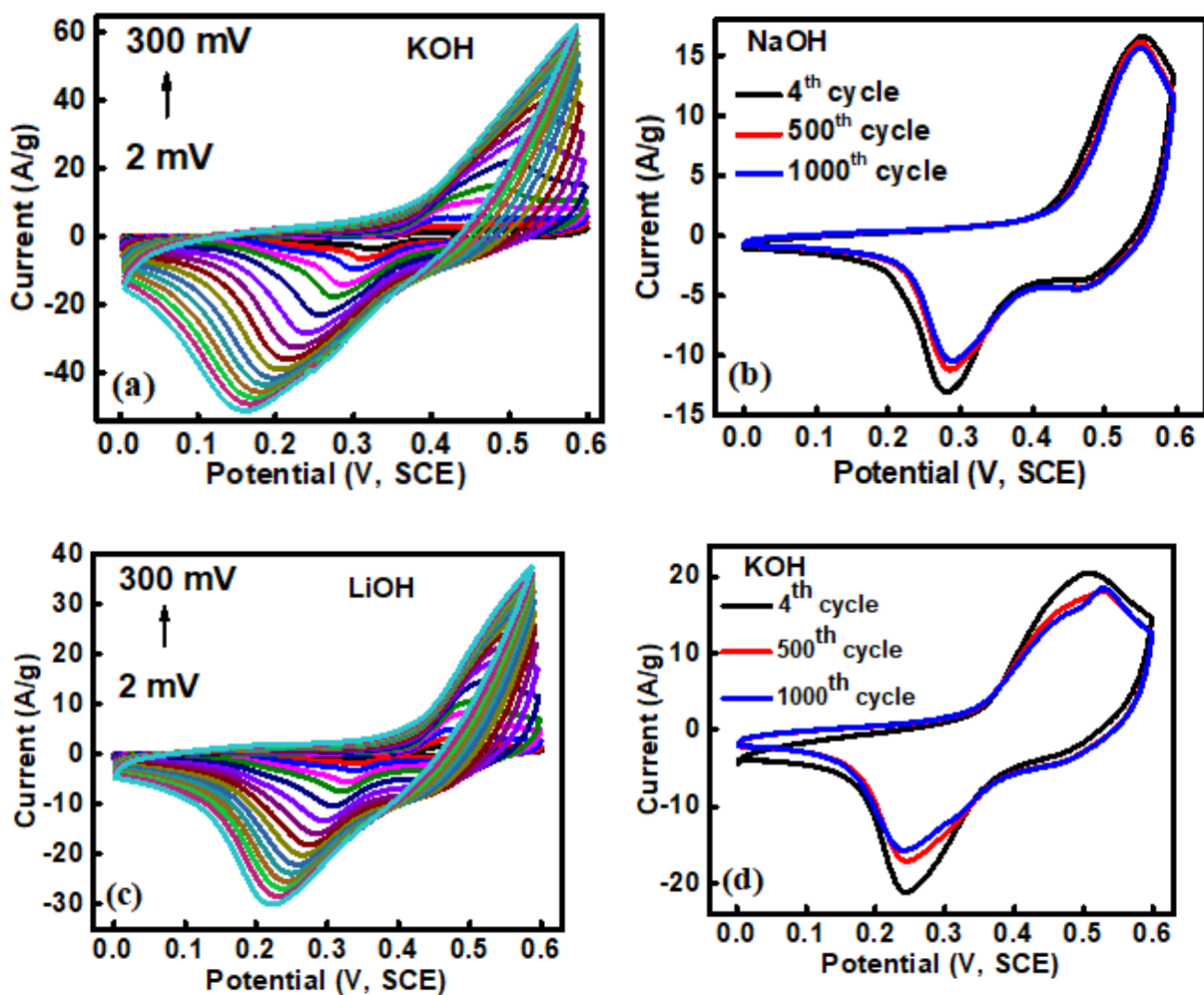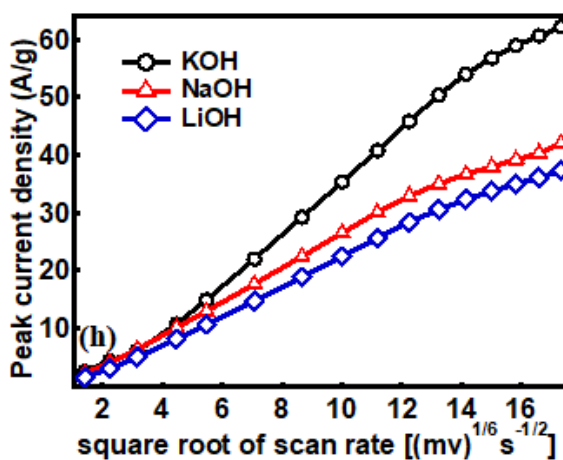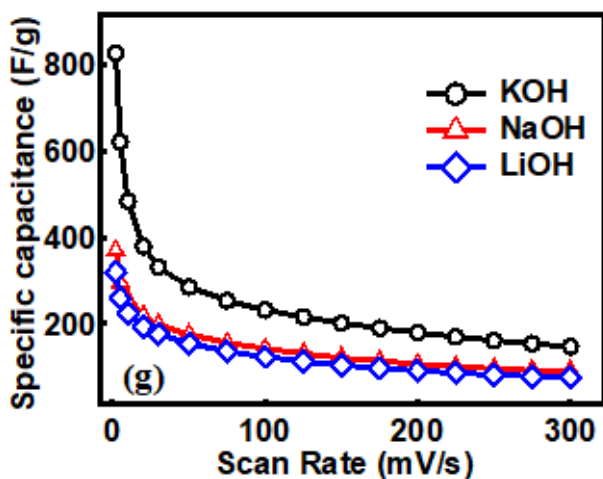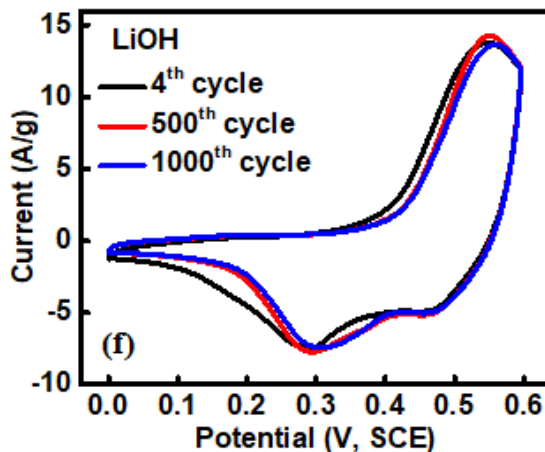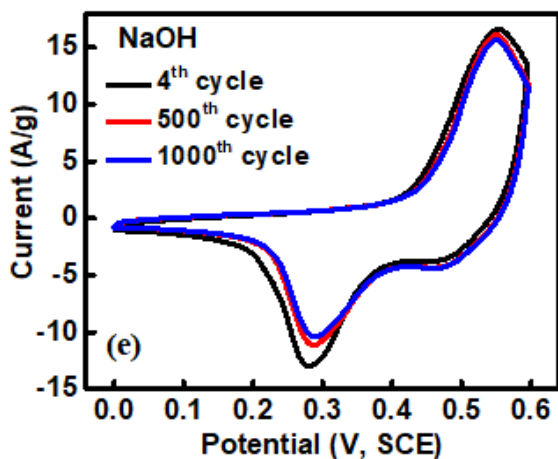
Figure 4.3 Cyclic voltammetry curves of tubular Co_3O_4 electrode obtained in the scan range of 5mV/s to 300 mV/s measured in (a) 3M KOH, (b) 3M NaOH, and (c) 3M LiOH electrolytes. Cyclic stability curves measured up to 1000 cycles in (d) KOH, (e)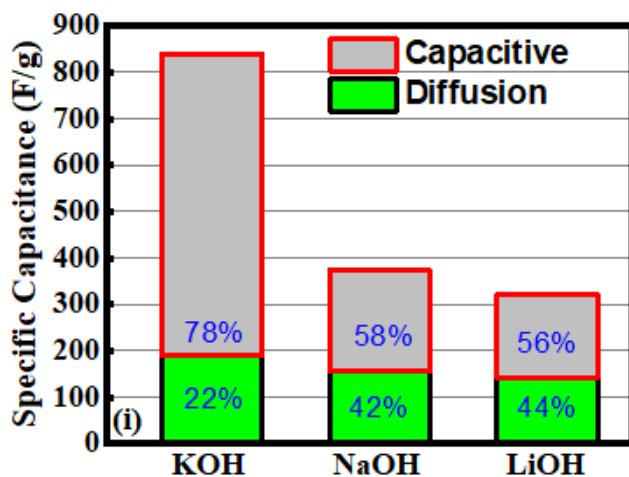 NaOH, and (f) LiOH electrolytes. (g) Specific capacitance vs. scan rate, (h) and peak current vs. (scan rate)$^{1/2}$, and (i) diffusion and capacitive contribution to the specific capacitance.

Figure 4.4 (a),(c) and (e) shows the galvanostatic charge-discharge (GCD) measurements performed in the voltage window of 0.0 to 0.6 V at different current densities between 0.75 A/g to 30 A/g in different electrolytes. The non-linearity between the potential and time indicates that the capacitance of the studied materials is not constant over the potential ranges both in charge and discharge cycle, as also confirmed by the CV curves. The specific capacitance of electrodes was calculated using the following equation:

$$C_{sp} = \frac{I \times t}{m \times \Delta V} \qquad …(4.7)$$

Where C_{sp} is the specific capacitance (F/g), I (A) is the charge-discharge current, ΔV (V) is the potential range, m (g) is the mass of the electroactive materials, and t (s) is the discharging time. The GCD curves with a plateau, usually displayed by oxide electrodes, show pseudocapacitive behavior of electrode with respect to their discharging time for all electrolytes. This GCD behavior could be originating from the electrochemical adsorption-desorption of electrolyte ions such as OH^- and/or a redox reaction on the electrode/electrolyte interface [103,104]. It is observed that the discharging time of biomorphic Co_3O_4 is much longer under KOH electrolyte. The specific capacitances of biomorphic Co_3O_4 at 1 A/g are 401.7817 F/g, 139.64 F/g, 132.35 F/g, for KOH, NaOH and LiOH electrolytes, respectively. The current density dependence of the specific capacitance of the electrode is exhibited in Figure 4.4 (g). The observed decrease in the capacitance with increasing discharge current density is likely caused by the increase in the

potential drop due to the resistance tubular Co_3O_4 and by the insufficient Faradic redox reaction of the active materials at higher discharge current densities. This implies that ions can penetrate the inner structure of the electrode material and gain access to almost all available active area of the electrode at lower current densities, but the effective use of the material is limited to only the outer surface of the electrode at higher current densities. The specific capacitance of bio-templated Co_3O_4 in this study is compared with the literature values at current density 0.5-1 A/g and scan rate 2-5 mV/s are listed in Table 4.1. It is evident from Table 4.1, that the observed specific capacitance value of bio-templated Co_3O_4 in this study is comparable or better than the values obtained via other templating mechanisms.

Table: 4.1: Comparison of sp. capacitance of electrodes derived using biomorphic templates.

Biotemplates	Electrode Material	Scan rate (mv/s)	Specific Cap. (Csp)	Current density (A/g)	Specific Cap. (Csp)	Reference
Chebula fruits				1	642 F/g	[105]
Cotton fiber				1	284 F/g	[106]
Sorghum straw	Co_3O_4			0.5	107 F/g	[20]
Wheat floors				0.5	161 F/g	[107]
Cotton fiber	Co_3O_4			0.5	130.5 F/g	[35]
Jack fruits				0.5	85 F/g	[108]
Biomass				0.5	892 F/g	[109]
pre-carbonized of fibers of oil palm empty fruit bunches		5	17.3F/g (1.5hr) 27.1F/g (2hr)			[110]
Green roots		2	383F/g(400$_0$C),456F/g(500$_0$C),296F/g (600$_0$C)			[111]
Table 4.1 continue						
Cotton fiber	Co_3O_4	2	828 F/g (aq. KOH)	0.75	448 F/g	[This study]

To estimate the electrochemical utilization of the active material in this study (RT- Co_3O_4 electrode), we calculated the fraction of cobalt sites, z, which can be gauged by Faraday's law using the following relationship [112]:

$$z = C_{sp}\, MW\, \Delta V/F \qquad \ldots(4.8)$$

Where *Csp* is the specific capacitance value, *MW* is the molecular weight, *ΔV* is the applied potential window, and *F* is the Faraday's constant. The value of *z* is 1 if all the electroactive material is involved in the redox process, that is, if all the cobalt sites have been reversibly participating in the oxidation-reduction process. The molecular weight of Co (84.03 g/mol) in Co_3O_4, the specific capacitance at a current density of 1 A/g (Csp~ 401.78 F/g) for KOH, Figure 4.4 (g), and a potential window of 0.6 V gives a *z* value of 0.209. In other words, ~20% of the total active material (cobalt atoms) participates in the redox reaction for the charge storage. While for NaOH and LiOH, the calculated value of *z* is 7.0% and 6.6 %, respectively. Overall, the low value of *z* suggests that the redox reaction for the charge storage in tubular Co_3O_4 structure occurs only at the surface of the Co_3O_4, with little bulk interaction because of diffusion of OH^- ions into the material. It could be concluded that the redox reaction for the charge storage in Co_3O_4 mostly occurs only at the redox sites predominantly located on the surface of the particles [68,113].

The Coulombic efficiency (η) of the devices was calculated from its charging (T_c) and the discharging (T_d) times from GCD curves following the relation, $\eta = T_d/T_c \times 100$, and is plotted in Figure 4.5(b), (d) and (f) as a function of cyclic time. The initial η of the device was ~100%, which remained practically the same in all three electrolytes even after 5,000 cycles. The cycling performance of electroactive material is a significant parameter to be studied for its practical applications. The cyclic performance of bio-templated Co_3O_4 nanostructure was carried out at a

current density of 10 A/g in KOH, NaOH, and LiOH, and is shown in Figure 5(b), (d), and (f).

Percentage retention in specific capacitance was calculated using,

% retention in specific capacitance = $(C_{\#}/C_1) \times 100$,   …(4.9)

Where $C_{\#}$ and C_1 is specific capacitance at various cycles and at the 1_{st} cycle, respectively. The

specific capacitance of the electrode is reduced by 18% in KOH, 42% in NaOH, and 35% in

LiOH. A gradual increase in the internal resistance could be attributed to the incomplete reversal

of the faradic process during the discharge process, thus lowering the retention rate of the

electrode [114,115].
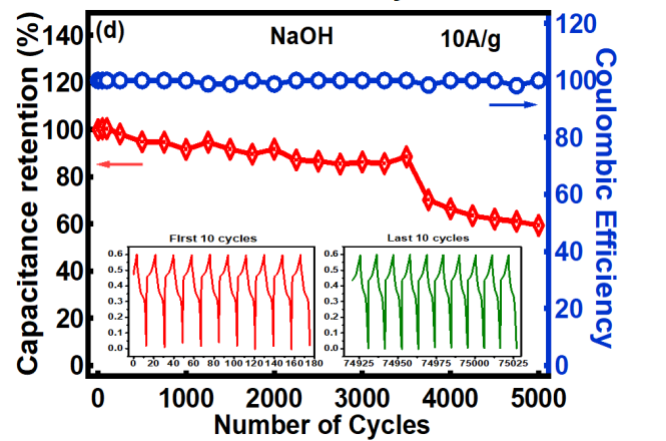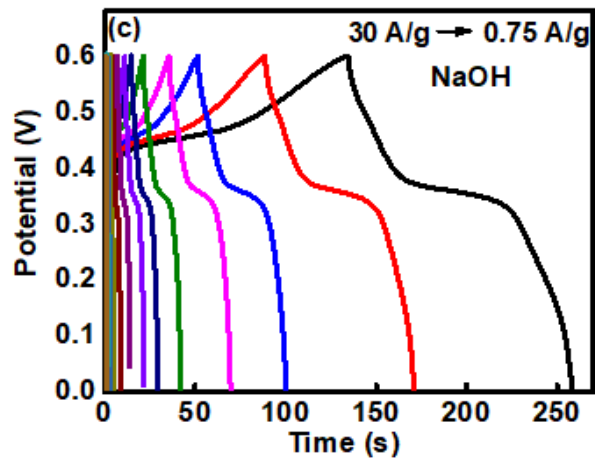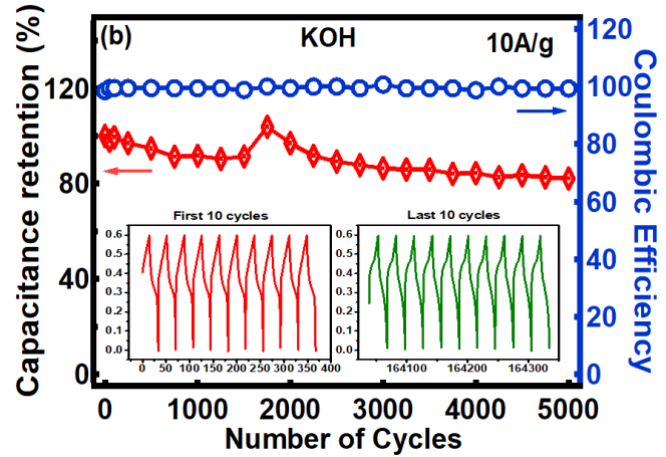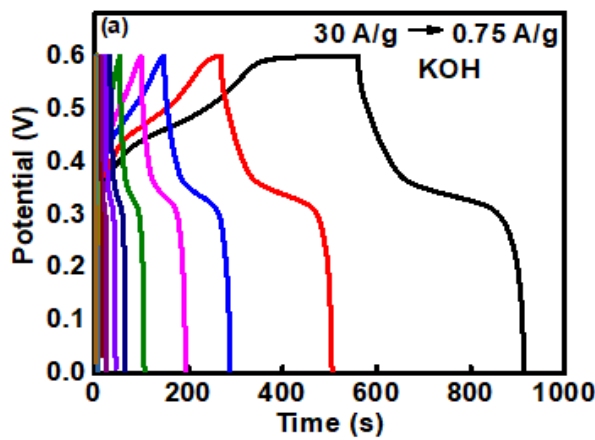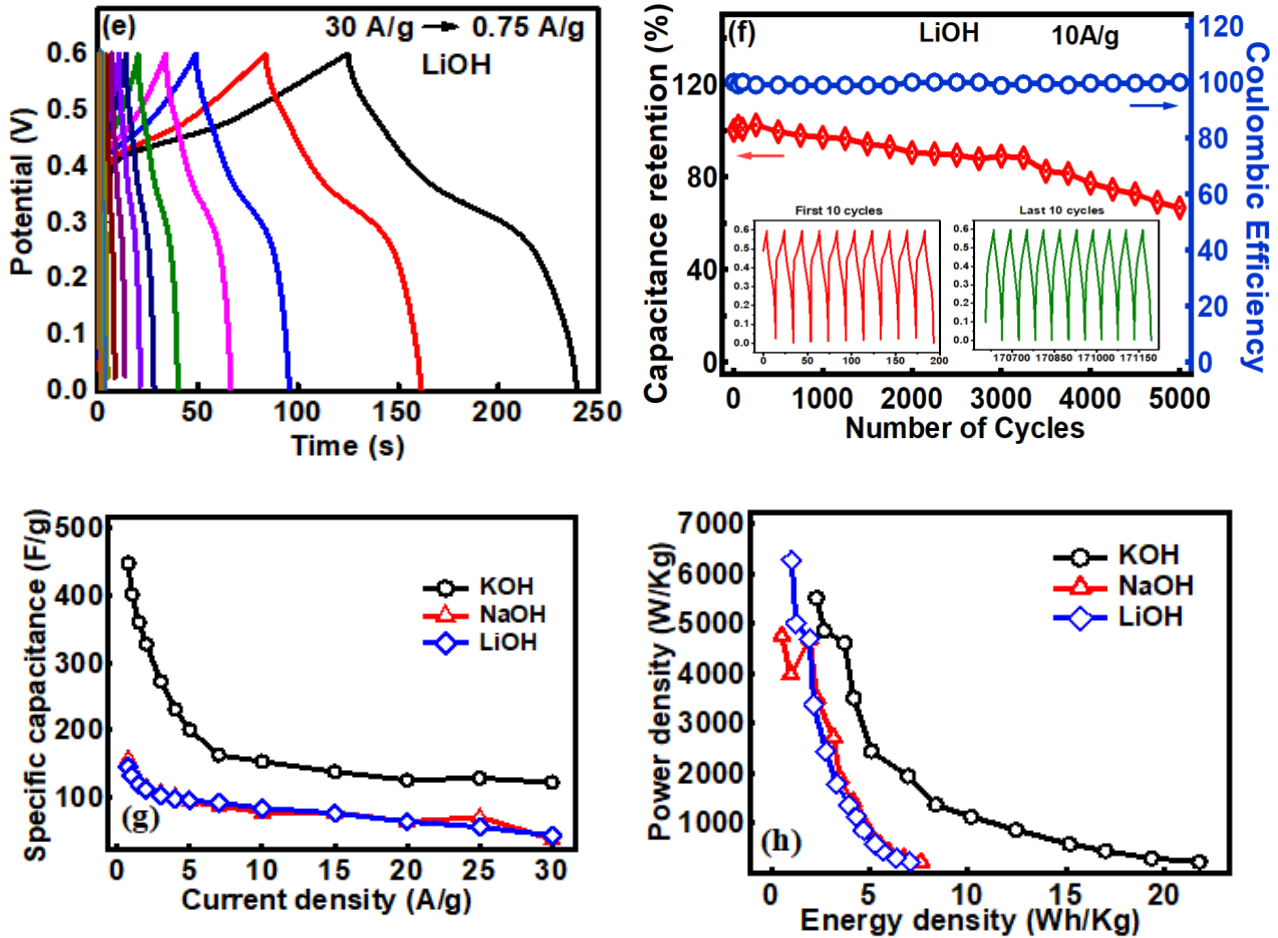
Figure 4.4 Charge-discharge curves of tubular Co_3O_4 electrode measured in the current density window of 0.75 to 30 A/g under different electrolytes (a) 3M KOH, (c) 3M NaOH, and (e) 3M LiOH. Cyclic stability and Coulombic efficiency tested at 1A/g current density for 5000 cycles in (b) 3M KOH, (d) 3M NaOH, and (f) 3M LiOH electrolytes. (g) Comparison of specific capacitance as a function of current density and (h) Ragone plot of power density vs. energy density.

Figure 4.5(h) shows Ragone plots of as-synthesized cobaltite. The energy densities (E) and power densities (P) of the electrochemical cells are calculated using the following equations [116]:

E=(1/2)CV$_2$ ... (4.10)

and

P=E/t,   ... (4.11)

Where *C* is the specific capacitance that depends on the mass of the electrodes, *V* is the operating voltage of the cell, and *t* is the discharge time in seconds. As known, the most important point for high-performance supercapacitors is to obtain a high energy density and meanwhile providing an outstanding power density. It is observed from Figure 4.5(h) that the tubular Co$_3$O$_4$ electrode display superior performance over energy density up to 22 Wh/kg, with a peak power density of up to 5,500 W/kg. However, LiOH displays a high power density of 6,500 W/kg at the lower end of the energy density spectrum.

The impedance spectra of tubular Co$_3$O$_4$ microstructure electrode was recorded with 10 mV AC perturbation in the frequency range from 0.05 Hz to 10 kHz in 3 M KOH, NaOH and LiOH electrolytes and are plotted in Figure 4.6. A suppressed semicircle exists in the higher frequency range followed by a rising line in the lower frequency range, where their behaviors are mainly capacitive. Usually, the depressed semicircles refer to small charge transfer resistances between electrode and electrolyte [117]. The diameter of the semicircle represents the kinetic resistance to the ion transfer, known as charge transfer resistance (R$_{ct}$) of the redox reactions. The R$_{ct}$ is rather low for the present tubular Co$_3$O$_4$; 0.39 Ω for LiOH, 0.39 Ω for NaOH, and 0.27 Ω for KOH, which is attributed to the improved ionic conduction and electrolyte diffusion through the pores of the electrode material [118]. The inclined line in the low-frequency region represents the Warburg impedance (Z$_w$), which is related to solid-state diffusion of positive ions in the electrode materials [119]. At the low-frequency region, the slope of the curve varies for

three electrolytes with KOH highest and followed by NaOH and LiOH. The high slope of the straight line of tubular Co_3O_4 in KOH electrolyte is further evidence for the fast ion diffusion behavior of K_+ in the tubular Co_3O_4 electrode.
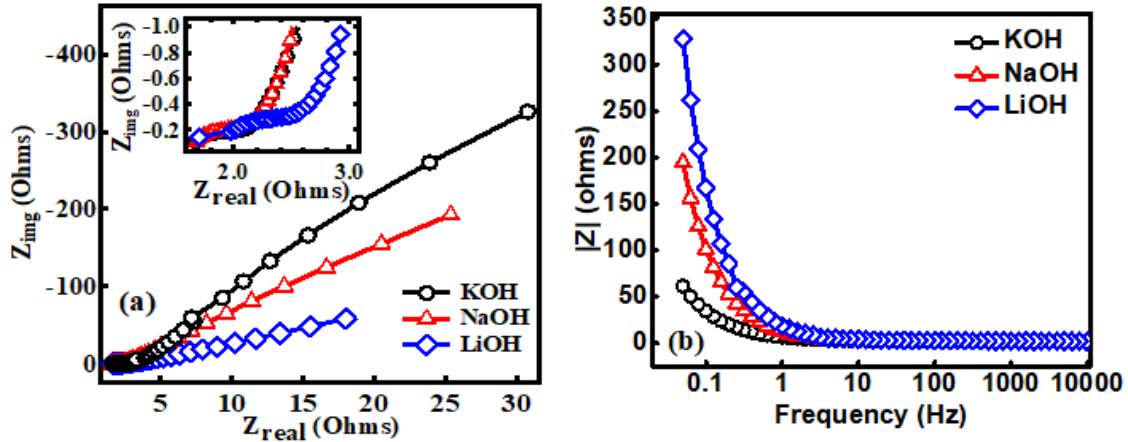
Figure 4.5 (a) Nyquist plot for tubular Co_3O_4 electrode at open circuit potential obtained in different electrolytes, and (b) frequency-dependent real impedance measured in different electrolytes.

Also, the low-frequency region (<1 Hz) of the second segment of the electrochemical impedance spectroscopy (EIS) curve indicates the electrically charged electrode-electrolyte interface that generates the supercapacitive behavior of the device. The characteristics of a supercapacitor, frequency-dependent capacitive behavior and power density could be evaluated from this segment of the EIS by expressing the total capacitance as a combination of real (C') and imaginary parts (C") [120,121].

$$C(\omega) = C'(\omega) + iC''(\omega) \qquad \text{...(4.12)}$$

$$C'(\omega) = -Z''(\omega)/\omega|Z|^2 \qquad \text{...(4.13)}$$

$$C''(\omega) = C'(\omega)/\omega|Z|^2 \qquad \dots(4.14)$$

The C' is a measure of the charge stored as a function frequency, representing the energy density and C'' corresponds to the energy dissipation occurring during charge storage. Fig. 4.7 shows the variation of C' and C'' as a function of frequency. The C' asymptotically decreases as frequency increases. The C' value electrode is lowest when measured in KOH while highest in LiOH electrolyte.

Furthermore, Figure 4.7 shows that the C'' displayed a bell-shaped curve with the frequency corresponding to the peak (fo) represents the point where the device changes from purely resistive to purely capacitive circuit 50 and is a measure of charge relaxation time (τ) defined by $\tau = 1/fo$. The τ quantitatively measures how fast a supercapacitor is discharged (i.e., power density). The behavior of the Co_3O_4 electrode in the three electrolytes is noticeably different, the fo determined from the graph are at 1 mHz in KOH, 1.25 mHz in NaOH, and 3.16 mHz in LiOH. The τ is calculated to be $1x10_3$ s, 800 s, 316s in 3M KOH, NaOH, and LiOH, respectively. i.e., the power capability of tubular Co_3O_4 electrode in LiOH is higher than that in either KOH or NaOH, consistent with the observations from GCD measurements, Figure 4.5(h).

The electrolyte within an electrochemical not only plays a fundamental role in the electrical double layer formation and the reversible redox process for the charge storage (in pseudocapacitors) but also determines the supercapacitor performance. The electrolyte nature, including (a) the ion type and size; (b) the ion concentration and solvent; (c) the interaction between the ion and the solvent; (d) the interaction between the electrolyte and the electrode materials; (e) mobility and diffusion coefficient of solvated ions, and (e) the potential window, all have an influence on the pseudocapacitance, the energy/power densities as well as the cycle-life. The superior performance of electrodes in KOH electrolyte can be understood in terms of

the molecular size of the hydrated ions and the molar conductance of electrolytes. As per the literature Li_+ with ionic radii, 0.6 Å is much smaller than Na_+ ionic radii of 0.95 Å and K_+ ionic radii of 1.33 Å [122,123]. This implies that Li_+ can easily intercalate compared to Na_+ and K_+. However, tubular Co_3O_4 electrodes display the highest specific capacitance in KOH, followed by NaOH and LiOH. This result, contrary to the expectation, is explained on the basis of the ionic radii of hydrated ions [124,125]. The smaller ions, in fact, form larger hydrated ions. The hydrated cation of Li_+ has ionic radii of 3.82 Å, which is larger than the hydrated cation ionic radii of Na_+ of 3.58 Å and hydrated cation ionic radii of K_+ of 3.31 Å [80]. Also, conductivity measurements performed by Ho et al. report that the conductance of KOH>NaOH>LiOH [126]. Thus smaller hydrated ionic radii of K_+ ions contributes to the higher ionic conductivity of the KOH electrolyte as compared to that of NaOH and LiOH. This leads to lower electrochemical series resistance and hence better conductivity [127]. On the other hand, Li_+ ions, due to their lower mobility and diffusion coefficient, remain close to the electrode-electrolyte interface during the charging-discharging process but ignoring large volume intercalation-deintercalation in the active material. Thus, from the above discussion, it is evident that not only the surface area, pore size, and density or electrode electronic characteristics are important, but the type of electrolytes play a significant role in determining the specific capacitance of the electrode. Also, the observed high specific capacitance of bio-templated tubular Co_3O_4 microstructure may also come from the presence of the activated carbon template as activated carbons made of biomass could result in (i) pseudocapacitive contribution, (ii) higher electron density, (iii) simultaneous activation.
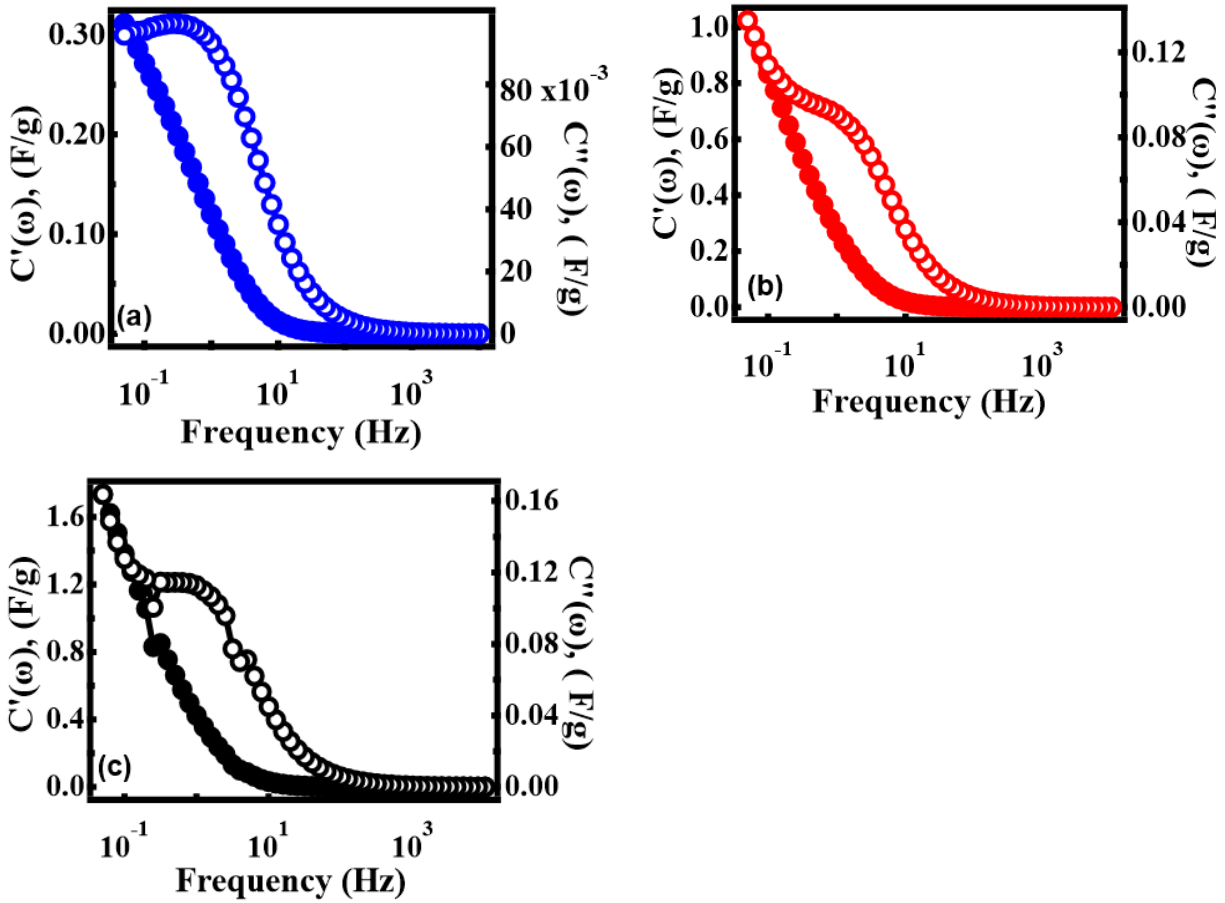
Figure 4.6 The variation of the real (C') and imaginary (C") part of the capacitance with the frequency at open circuit potential for (a) 3M KOH, (b) 3M NaOH, and (c) 3 M LiOH electrolytes.

CHAPTER 5

Conclusion

In conclusion, the facile synthesis of tubular Co_3O_4 nanostructure using cotton as a bio-template is demonstrated—the as-synthesized tubular Co_3O_4 with the outer diameter 9.02μm displays excellent crystallinity and phase purity. The tubular Co_3O_4 electrodes display desirable electrochemical properties for the fabrication of high-performance supercapacitor devices. A supercapacitor electrode fabricated using the tubular Co_3O_4 demonstrate a record specific capacitance, accounting ~828 F/g at 2 mV/s scan rate and around 401 F/g at 1 A/g current density when evaluated in KOH electrolyte. The electrochemical cyclic charge-discharge and voltammogram showed excellent Coulombic stability up to 5,000 cycles. Overall, tubular Co_3O_4 electrodes displayed superior performance, high power (5,500 W/kg) and energy density (22 Wh/kg), when tested under KOH electrolyte as compared to the other two. The superior electrochemical performance of the templated tubular Co_3O_4 microstructure in KOH electrolyte is attributed to its high surface area, appropriate pore size and pore distribution, activated carbon template, and the smaller hydrated cationic radii of K_+, which all allow the easy mass transfer of ions through the electrode.

Future Work:

Further work of Co_3O_4 is necessary to understand it's electrocapacitive property;

a) Preparation of Co_3O_4 with different external parameters (temperature, time) to compare there role on specific capacitance.

b) Theoritical study of Co_3O_4 to calculate electrical conductivity.

Acknowledgment

References:

1. Alqahtani, D., 2017. Effect of Metal Ion Substitution on Electrochemical Properties of Cobalt Oxide for Energy Applications.
2. Cericola, D. and Kötz, R., 2012. Hybridization of rechargeable batteries and electrochemical capacitors: Principles and limits. *Electrochimica Acta*, *72*, pp.1-17
3. Zhang, T., Zhang, F., Zhang, L., Lu, Y., Zhang, Y., Yang, X., Ma, Y. and Huang, Y., 2015. High energy density Li-ion capacitor assembled with all graphene-based electrodes. *Carbon, 92,* pp.106-118
4. Vangari, M., Pryor, T. and Jiang, L., 2013. Supercapacitors: review of materials and fabrication methods. *Journal of Energy Engineering*, *139*(2), pp.72-79
5. Zhao, X., Sánchez, B.M., Dobson, P.J. and Grant, P.S., 2011. The role of nanomaterials in redox-based supercapacitors for next generation energy storage devices. *Nanoscale*, *3*(3), pp.839-855.
6. Venkataraman, A., 2015. Pseudocapacitors for energy storage.
7. https://www.explainthatstuff.com/batteries.html
8. Zhang, T., Zhang, F., Zhang, L., Lu, Y., Zhang, Y., Yang, X., Ma, Y. and Huang, Y., 2015. High energy density Li-ion capacitor assembled with all graphene-based electrodes. *Carbon*, *92*, pp.106-118.
9. https://americanhistory.si.edu/fuelcells/basics.htm
10. Yilmaz, A.E. and Ispirli, M.M., 2015. An investigation on the parameters that affect the performance of hydrogen fuel cell. *Procedia-Social and Behavioral Sciences*, *195*, pp.2363-2369.
11. https://www.rs-online.com/designspark/powering-electric-vehicles-fuel-cells-and-big-batteries
12. https://en.wikipedia.org/wiki/Supercapacitor
13. Halper, M.S. and Ellenbogen, J.C., 2006. Supercapacitors: A brief overview. *The MITRE Corporation, McLean, Virginia, USA*, pp.1-34
14. https://electronicsforu.com/resources/learn-electronics/supercapacitors-fundamentals-applications
15. https://en.wikipedia.org/wiki/Supercapacitor.
16. Wang, H. and Pilon, L., 2012. Physical interpretation of cyclic voltammetry for measuring electric double layer capacitances. *Electrochimica Acta*, *64*, pp.130-139.
17. Safitri, N., 2019, June. Different Trends of Hybrid Solar And Raindrops Energies to Generate Photovoltaic. In *IOP Conference Series: Materials Science and Engineering* (Vol. 536, No. 1, p. 012058). IOP Publishing.
18. Conway, B.E. "Electrochemical supercapacitors scientific fundamentals and technological applications." 1999, 17-28.
19. https://en.wikipedia.org/wiki/Underpotential_deposition
20. Finnefrock, A.C., 1998. *Time-resolved Measurements of the underpotential deposition of copper onto platinum (111) in the presence of chloride*. Cornell University
21. Wang, Z., Zhang, X., Zhang, Z., Qiao, N., Li, Y. and Hao, Z., 2015. Hybrids of $NiCo_2O_4$ nanorods and nanobundles with graphene as promising electrode materials for supercapacitors. *Journal of colloid and interface science, 460*, pp.303-309.
22. Du, N., Zhang, H., Chen, B.D., Wu, J.B., Ma, X.Y., Liu, Z.H., Zhang, Y.Q., Yang, D.R.,

Huang, X.H. and Tu, J.P., 2007. Porous Co_3O_4 Nanotubes Derived from $Co_4(CO)_{12}$ Clusters on Carbon Nanotube Templates: A Highly Efficient Material For Li-Battery Applications. *Advanced Materials*, *19*(24), pp.4505-4509.

23. Augustyn, V., Simon, P. and Dunn, B., 2014. Pseudocapacitive oxide materials for high-rate electrochemical energy storage. *Energy & Environmental Science*, *7*(5), pp.1597-1614.

24. Guo, F., Gupta, N. and Teng, X., 2018. Enhancing Pseudocapacitive Process for Energy Storage Devices: Analyzing the Charge Transport Using Electro-kinetic Study and Numerical Modeling. *Supercapacitors: Theoretical and Practical Solutions*, p.87

25. Feng, G., Qiao, R., Huang, J., Sumpter, B.G. and Meunier, V., 2010, August. Computational modeling of carbon nanostructures for energy storage applications. In *10th IEEE International Conference on Nanotechnology* (pp. 100-104). IEEE.

26. https://www.mouser.com/applications/new-supercapacitor-applications/

27. Muzaffar, A., Ahamed, M.B., Deshmukh, K. and Thirumalai, J., 2019. A review on recent advances in hybrid supercapacitors: Design, fabrication and applications. *Renewable and Sustainable Energy Reviews*, *101*, pp.123-145.

28. Bera, G., Sinha, S., Rambabu, P., Das, P., Gupta, A.K. and Turpu, G.R., 2016, May. Structural characterization of $FeVO_4$ synthesized by co-precipitation method. In *AIP Conference Proceedings*, *1728(1)*, p. 020284.

29. Zhang, J., Sun, Y., Li, X. and Xu, J., 2020. Fabrication of $NiCo_2O_4$ nanobelt by a chemical co-precipitation method for non-enzymatic glucose electrochemical sensor application. *Journal of Alloys and Compounds*, p.154796

30. Ahmad, S., Yang, C., Xie, W., Deng, Z., Zhang, H., Zhao, Y. and Su, X., 2020. Molten salt-templated synthesis of ternary $NiS–NiCo_2O_4$@ C composites as high performance catalysts for 4-nitro phenol reduction and supercapacitor. *Carbon*, *158*, pp.912-921

31. An, C., Wang, Y., Huang, Y., Xu, Y., Jiao, L. and Yuan, H., 2014. Porous $NiCo_2O_4$ nanostructures for high performance supercapacitors via a microemulsion technique. *Nano Energy, 10*, pp.125-134.

32. Raistrick, I.D. and Sherman, R.J., 1987. Electrical response of electrochemical capacitors based on high surface area ruthenium oxide electrodes. In *Electrode materials and processes for energy conversion and storage*.

33. Tong, R.R., Mason, G.E., Lee, H.L. and Bullard, G.L., 1988. Power source characteristics of the ultracapacitor. *33rd International Power Sources Symposium*, pp. 600-606.

34. Trasatti, S. and Buzzanca, G., 1971. Ruthenium dioxide: a new interesting electrode material.
Solid state structure and electrochemical behaviour. *Journal of Electroanalytical Chemistry and Interfacial Electrochemistry*, *29*(2), pp.A1-A5

35. Bi, R.R., Wu, X.L., Cao, F.F., Jiang, L.Y., Guo, Y.G. and Wan, L.J., 2010. Highly dispersed RuO_2 nanoparticles on carbon nanotubes: facile synthesis and enhanced supercapacitance performance. The *Journal of Physical Chemistry C, 114*(6), pp.2448-2451

36. Hu, C.C., Chang, K.H., Lin, M.C. and Wu, Y.T., 2006. Design and tailoring of the nanotubular arrayed architecture of hydrous RuO_2 for next generation supercapacitors. *Nano letters*, *6*(12), pp.2690-2695

37. Chen, P., Chen, H., Qiu, J. and Zhou, C., 2010. Inkjet printing of single-walled carbon nanotube/RuO_2 nanowire supercapacitors on cloth fabrics and flexible substrates. *Nano Research*, *3*(8), pp.594-603.

38. Liu, Y., Zhao, W. and Zhang, X., 2008. Soft template synthesis of mesoporous $Co_3O_4/RuO_2\cdot xH_2O$ composites for electrochemical capacitors. *Electrochimica Acta*, *53*(8), pp.3296-3304

39. Gujar, T.P., Kim, W.Y., Puspitasari, I., Jung, K.D. and Joo, O.S., 2007. Electrochemically deposited nanograin ruthenium oxide as a pseudocapacitive electrode. *Int. J. Electrochem. Sci*, *2*, pp.666-673

40. Zhang, X., Shi, W., Zhu, J., Zhao, W., Ma, J., Mhaisalkar, S., Maria, T.L., Yang, Y., Zhang, H., Hng, H.H. and Yan, Q., 2010. Synthesis of porous NiO nanocrysals with controllable surface area and their application as supercapacitor electrodes. *Nano Research*, *3*(9), pp.643-652

41. Nam, K.W. and Kim, K.B., 2002. A study of the preparation of NiO_x electrode via electrochemical route for supercapacitor applications and their charge storage mechanism. *Journal of the Electrochemical Society*, *149*(3), pp.A346-A354

42. Pang, S.C., Anderson, M.A. and Chapman, T.W., 2000. Novel electrode materials for thin-film ultracapacitors: comparison of electrochemical properties of sol-gel-derived and electrodeposited manganese dioxide. *Journal of the Electrochemical Society*, *147*(2), pp.444-450.

43. Chen, P.C., Shen, G., Shi, Y., Chen, H. and Zhou, C., 2010. Preparation and characterization of flexible asymmetric supercapacitors based on transition-metal-oxide nanowire/single-walled carbon nanotube hybrid thin-film electrodes. *ACS nano*, *4*(8), pp.4403-4411

44. Du, X., Wang, C., Chen, M., Jiao, Y. and Wang, J., 2009. Electrochemical performances of nanoparticle Fe_3O_4/activated carbon supercapacitor using KOH electrolyte solution. *The Journal of Physical Chemistry C, 113*(6), pp.2643-2646

45. Yuan, C., Li, J., Hou, L., Zhang, X., Shen, L. and Lou, X.W., 2012. Ultrathin mesoporous $NiCo_2O_4$ nanosheets supported on Ni foam as advanced electrodes for supercapacitors. *Advanced Functional Materials*, *22*(21), pp.4592-4597.

46. Cheng, J., Lu, Y., Qiu, K., Yan, H., Hou, X., Xu, J., Han, L., Liu, X., Kim, J.K. and Luo, Y., 2015. Mesoporous $ZnCo_2O_4$ nanoflakes grown on nickel foam as electrodes for high performance supercapacitors. *Physical Chemistry Chemical Physics, 17*(26), pp.17016-17022

47. Mondal, A.K., Su, D., Chen, S., Ung, A., Kim, H.S. and Wang, G., 2015. Mesoporous $MnCo_2O_4$ with a flake-like structure as advanced electrode materials for lithium-ion batteries and supercapacitors. *Chemistry–A European Journal*, *21*(4), pp.1526-1532

48. Wang, Z., Jia, W., Jiang, M., Chen, C. and Li, Y., 2016. One-step accurate synthesis of shell controllable $CoFe_2O_4$ hollow microspheres as high-performance electrode materials in supercapacitor. *Nano Research, 9*(7), pp.2026-2033.

49. Zuo, Y., Ni, J.J., Song, J.M., Niu, H.L., Mao, C.J., Zhang, S.Y. and Shen, Y.H., 2016. Synthesis of Co_3O_4/NiO nanofilms and their enhanced electrochemical performance for supercapacitor application. *Applied Surface Science, 370*, pp.528-535

50. Chabi, S., Peng, C., Hu, D. and Zhu, Y., 2014. Ideal three-dimensional electrode structures for electrochemical energy storage. *Advanced Materials, 26*(15), pp.2440-2445.

51. Li, L., He, F., Gai, S., Zhang, S., Gao, P., Zhang, M., Chen, Y. and Yang, P., 2014. Hollow structured and flower-like C@ $MnCo_2O_4$ composite for high electrochemical performance in a supercapacitor. *CrystEngComm, 16*(42), pp.9873-9881

52. Cheng, G., Kou, T., Zhang, J., Si, C., Gao, H. and Zhang, Z., 2017. O22-/O-functionalized oxygen-deficient Co_3O_4 nanorods as high performance supercapacitor electrodes and electrocatalysts towards water splitting. *Nano Energy, 38*, pp.155-166

53. Zasada, F., Piskorz, W., Stelmachowski, P., Kotarba, A., Paul, J.F., Płociński, T., Kurzydłowski, K.J. and Sojka, Z., 2011. Periodic DFT and HR-STEM studies of surface structure and morphology of cobalt spinel nanocrystals. Retrieving 3D shapes from 2D images. *The Journal of Physical Chemistry C*, *115*(14), pp.6423-6432.

54. Kormondy, K.J., Posadas, A.B., Slepko, A., Dhamdhere, A., Smith, D.J., Mitchell, K.N., Willett-Gies, T.I., Zollner, S., Marshall, L.G., Zhou, J. and Demkov, A.A., 2014. Epitaxy of polar semiconductor Co_3O_4 (110): Growth, structure, and characterization. *Journal of Applied Physics*, *115*(24), p.243708

55. Xu, X.L., Chen, Z.H., Li, Y., Chen, W.K. and Li, J.Q., 2009. Bulk and surface properties of spinel Co_3O_4 by density functional calculations. *Surface Science*, *603*(4), pp.653-658

56. Sun, D., He, L., Chen, R., Liu, Y., Lv, B., Lin, S. and Lin, B., 2019. *Applied Surface Science, 465*, 232-240

57. Yan, D., Zhang, H., Chen, L., Zhu, G., Li, S., Xu, H. and Yu, A., 2014. *ACS applied materials & interfaces, 6*(18),15632-15637.

58. Liu, Y., Lv, B., Li, P., Chen, Y., Gao, B. and Lin, B., 2018. *Materials Letters, 210, 231-234.*

59. Edison, T.N.J.I., Atchudan, R., Sethuraman, M.G. and Lee, Y.R., 2016. *Journal of the Taiwan Institute of Chemical Engineers, 68*, 489-495.

60. Shi, Z., Xing, L., Liu, Y., Gao, Y. and Liu, J., 2018. *Carbon, 129*, pp.819-825.

61 . Balasubramanian, S. and Kamaraj, P.K., 2015. *Electrochimica Acta, 168*, 50-58.

62. Wang, G., Shen, X., Horvat, J., Wang, B., Liu, H., Wexler, D. and Yao, J., 2009. *J. Phys. Chem.C, 113*(11), 4357-4361.

63. Xu, J., Gao, L., Cao, J., Wang, W. and Chen, Z., 2010. *Electrochimica Acta, 56*(2), pp.732-736

64. Cui, L., Li, J. and Zhang, X.G., 2009 *Journal of applied electrochemistry, 39*(10), p.1871

65. Gao, Y., Chen, S., Cao, D., Wang, G. and Yin, J., 2010. Electrochemical capacitance of Co_3O_4 nanowire arrays supported on nickel foam. *Journal of Power Sources, 195*(6), pp.1757-1760

66. https://upload.wikimedia.org/wikipedia/commons/d/df/Bragg_legea.jpg

67. Guragain, D., Zequine, C., Poudel, T., Neupane, D., Gupta, R.K. and Mishra, S.R., 2020. Influence of Urea on the Synthesis of $NiCo_2O_4$ Nanostructure: Morphological and Electrochemical Studies. *Journal of nanoscience and nanotechnology*, *20*(4), pp.2526-2537.

68. B. D. Cullity, *Elements of X-ray Diffractoin (Addison-Wesley Publishing, Inc. 2nd Edition,* 1978

69. Lin, H.K., Chiu, H.C., Tsai, H.C., Chien, S.H. and Wang, C.B., 2003. Synthesis, characterization and catalytic oxidation of carbon monoxide over cobalt oxide. *Catalysis Letters*, *88*(3-4), pp.169-174.

70. Spencer, C.D. and Schroeer, D., 1974. Mössbauer study of several cobalt spinels using Co^{57} and Fe^{57}. *Physical Review B*, *9*(9), p.3658-3665.

71. Kurtulus, F. and Guler, H., 2005. A Simple Microwave-Assisted Route to Prepare Black Cobalt, Co_3O_4. *Inorganic Materials*, *41*(5), pp.483-485.

72. St G, C., Stoyanova, M., Georgieva, M. and Mehandjiev, D., 1999. Preparation and characterization of a higher cobalt oxide. *Materials Chemistry and Physics*, *60*(1), pp.39-43.

73. Štěpánek, F., Marek, M. and Adler, P.M., 1999. Modeling capillary condensation hysteresis cycles in reconstructed porous media. *AICHE Journal*, *45*(9), pp.1901-1912.

74. Yan, D., Zhang, H., Chen, L., Zhu, G., Li, S., Xu, H. and Yu, A., 2014. Biomorphic synthesis of mesoporous Co_3O_4 microtubules and their pseudocapacitive performance. *ACS Applied Materials & Interfaces*, 6(18), pp.15632-15637.

75. Largeot, C., Portet, C., Chmiola, J., Taberna, P.L., Gogotsi, Y. and Simon, P., 2008. Relation between the ion size and pore size for an electric double-layer capacitor. *Journal of the American Chemical Society*, *130*(9), pp.2730-2731.

76. Kuyucak, S., Andersen, O.S. and Chung, S.H., 2001. Models of permeation in ion channels. *Reports on Progress in Physics*, *64*(11), p.1427-1472.

77. Largeot, C., Portet, C., Chmiola, J., Taberna, P.L., Gogotsi, Y. and Simon, P., 2008. Relation between the ion size and pore size for an electric double-layer capacitor. *Journal of the American Chemical Society*, *130*(9), pp.2730-2731.

78. Zhi, J., Wang, Y., Deng, S. and Hu, A., 2014. Study on the relation between pore size and supercapacitance in mesoporous carbon electrodes with silica-supported carbon nanomembranes. *RSC Advances*, *4*(76), pp.40296-40300.

79. Kondrat, S., Perez, C.R., Presser, V., Gogotsi, Y. and Kornyshev, A.A., 2012. Effect of pore size and its dispersity on the energy storage in nanoporous supercapacitors. *Energy & Environmental Science*, *5*(4), pp.6474-6479.

80. Wang, R., Li, Q., Cheng, L., Li, H., Wang, B., Zhao, X.S. and Guo, P., 2014. Electrochemical properties of manganese ferrite-based supercapacitors in aqueous electrolyte: the effect of ionic radius. Colloids and Surfaces A: *Physicochemical and Engineering Aspects*, *457*, pp.94-99.

81. Hou, L., Yuan, C., Yang, L., Shen, L., Zhang, F. and Zhang, X., 2011. Urchin-like Co_3O_4 microspherical hierarchical superstructures constructed by one-dimension nanowires toward electrochemical capacitors. *RSC Advances*, *1*(8), pp.1521-1526.

82. Tong, G., Liu, Y. and Guan, J., 2014. In situ gas bubble-assisted one-step synthesis of polymorphic Co_3O_4 nanostructures with improved electrochemical performance for lithium ion batteries. *Journal of Alloys and Compounds*, *601*, pp.167-174.

83. Brousse, T. and Bélanger, D., 2003. A Hybrid Fe_3O_4 MnO_2 Capacitor in Mild Aqueous Electrolyte. *Electrochemical and Solid-State Letters*, *6*(11), pp.A244-A248.

84. Wang, S.Y., Ho, K.C., Kuo, S.L. and Wu, N.L., 2006. Investigation on capacitance mechanisms of Fe_3O_4 electrochemical capacitors. *Journal of the Electrochemical Society*, *153*(1), pp.A75-A80.

85. Tiruye, G.A., Munoz-Torrero, D., Palma, J., Anderson, M. and Marcilla, R., 2015. All-solid state supercapacitors operating at 3.5 V by using ionic liquid based polymer electrolytes. *Journal of Power Sources*, *279*, pp.472-480.

86. Gao, F., Shao, G., Qu, J., Lv, S., Li, Y. and Wu, M., 2015. Tailoring of porous and nitrogen-rich carbons derived from hydrochar for high-performance supercapacitor electrodes. *Electrochimica Acta*, *155*, pp.201-208.

87. Selvam, M., Srither, S.R., Saminathan, K. and Rajendran, V., 2015. Chemically and electrochemically prepared graphene/MnO_2 nanocomposite electrodes for zinc primary cells: a comparative study. *Ionics*, *21*(3), pp.791-799.

88. Tang, Y., Liu, Y., Yu, S., Gao, F. and Zhao, Y., 2015. Comparative study on three commercial carbons for supercapacitor applications. *Russian Journal of Electrochemistry*, *51*(1), pp.77-85.

89. Sankar, K.V. and Selvan, R.K., 2015. Improved electrochemical performances of reduced graphene oxide based supercapacitor using redox additive electrolyte. *Carbon*, *90*, pp.260-273.

90. Sahu, V., Shekhar, S., Sharma, R.K. and Singh, G., 2015. Ultrahigh performance supercapacitor from lacey reduced graphene oxide nanoribbons. *ACS Applied Materials & Interfaces*, *7*(5), pp.3110-3116.

91. Xiao, J. and Yang, S., 2011. Sequential crystallization of sea urchin-like bimetallic (Ni, Co) carbonate hydroxide and its morphology conserved conversion to porous $NiCo_2O_4$ spinel for pseudocapacitors. *RSC Advances*, *1*(4), pp.588-595.

92. Liu, X., Long, Q., Jiang, C., Zhan, B., Li, C., Liu, S., Zhao, Q., Huang, W. and Dong, X., 2013. Facile and green synthesis of mesoporous Co_3O_4 nanocubes and their applications for supercapacitors. *Nanoscale*, *5*(14), pp.6525-6529.

93. Hu, C.C., Chen, J.C. and Chang, K.H., 2013. Cathodic deposition of $Ni(OH)_2$ and $Co(OH)_2$ for asymmetric supercapacitors: importance of the electrochemical reversibility of redox couples. *Journal of Power Sources*, *221*, pp.128-133.

94. Ghosh, D., Giri, S. and Das, C.K., 2014. Hydrothermal synthesis of platelet β-$Co(OH)_2$ and Co_3O_4: Smart electrode material for energy storage application. *Environmental Progress & Sustainable Energy*, *33*(3), pp.1059-1064.

95. Zhu, T., Chen, J.S. and Lou, X.W., 2010. Shape-controlled synthesis of porous Co_3O_4 nanostructures for application in supercapacitors. *Journal of Materials Chemistry*, *20*(33), pp.7015-7020.

96. Xu, J., Gao, L., Cao, J., Wang, W. and Chen, Z., 2010. Preparation and electrochemical capacitance of cobalt oxide (Co_3O_4) nanotubes as supercapacitor material. *Electrochimica Acta, 56*(2), pp.732-736.

97. B. E. Conway, 1997. in "*Electrochemical Supercapacitors*" Kluwer Academic/Plenum Publishers, NewYork.

98. Yi, H., Wang, H., Jing, Y., Peng, T. and Wang, X., 2015. Asymmetric supercapacitors based on carbon nanotubes@ NiO ultrathin nanosheets core-shell composites and MOF-derived porous carbon polyhedrons with super-long cycle life. *Journal of Power Sources*, *285*, pp.281-290.

99. Augustyn, V., Come, J., Lowe, M.A., Kim, J.W., Taberna, P.L., Tolbert, S.H., Abruña, H.D., Simon, P. and Dunn, B., 2013. High-rate electrochemical energy storage through Li+ intercalation pseudocapacitance. *Nature Materials*, *12*(6), p.518.

100. Lindström, H., Södergren, S., Solbrand, A., Rensmo, H., Hjelm, J., Hagfeldt, A. and Lindquist, S.E., 1997. Li^+ ion insertion in TiO_2 (anatase). 1. Chronoamperometry on CVD films and nanoporous films. *The Journal of Physical Chemistry B*, *101*(39), pp.7710-7716.

101. Liu, T.C., Pell, W.G., Conway, B.E. and Roberson, S.L., 1998. Behavior of molybdenum nitrides as materials for electrochemical capacitors comparison with ruthenium oxide. *Journal of the Electrochemical Society*, *145*(6), pp.1882-1888

102. Wang, J., Polleux, J., Lim, J. and Dunn, B., 2007. Pseudocapacitive contributions to electrochemical energy storage in TiO_2 (anatase) nanoparticles. *The Journal of Physical Chemistry C*, *111*(40), pp.14925-14931.

103. Zhao, D.D., Bao, S.J., Zhou, W.J. and Li, H.L., 2007. Preparation of hexagonal nanoporous nickel hydroxide film and its application for electrochemical capacitor. *Electrochemistry Communications*, *9*(5), pp.869-874.

104. Sugimoto, W., Iwata, H., Yasunaga, Y., Murakami, Y. and Takasu, Y., 2003. Preparation of ruthenic acid nanosheets and utilization of its interlayer surface for electrochemical energy storage. *Angewandte Chemie International Edition*, *42*(34), pp.4092-4096.

105. Edison, T.N.J.I., Atchudan, R., Sethuraman, M.G. and Lee, Y.R., 2016. Supercapacitor performance of carbon supported Co_3O_4 nanoparticles synthesized using Terminalia chebula fruit. *Journal of the Taiwan Institute of Chemical Engineers*, *68*, pp.489-495.

106. Sun, D., He, L., Chen, R., Liu, Y., Lv, B., Lin, S. and Lin, B., 2019. Biomorphic composites composed of octahedral Co_3O_4 nanocrystals and mesoporous carbon microtubes templated from cotton for excellent supercapacitor electrodes. *Applied Surface Science*, *465*, pp.232-240.

107. Cui, Z., Gao, X., Wang, J., Yu, J., Dong, H., Zhang, Q., Yu, L. and Dong, L., 2018. Synthesis and Supercapacitance of Co_3O_4 Supported on Porous Carbon Derived from Wheat Flour. *ECS Journal of Solid State Science and Technology*, *7*(10), pp.M161-M165.

108. Sennu, P., Aravindan, V. and Lee, Y.S., 2016. High energy asymmetric supercapacitor with 1D@ 2D structured $NiCo_2O_4@Co_3O_4$ and jackfruit derived high surface area porous carbon. *Journal of Power Sources*, *306*, pp.248-257.

109. Shi, Z., Xing, L., Liu, Y., Gao, Y. and Liu, J., 2018. A porous biomass-based sandwich-structured Co_3O_4@Carbon Fiber@Co_3O_4 composite for high-performance supercapacitors. *Carbon*, *129*, pp.819-825.

110. Awitdrus, A., 2016. Cyclic Voltammometry of Binderless Activated Carbon Monoliths based supercapacitor from Mixtures of Pre-carbonized of Fibers of Empty Fruit Bunches and Green Petroleum Coke. *Knowledge Engineering*, *1*(1), pp. 1-8.

111. Balasubramanian, S. and Kamaraj, P.K., 2015. Fabrication of natural polymer assisted mesoporous Co_3O_4/carbon composites for supercapacitors. *Electrochimica Acta*, *168*, pp.50-58.

112. Srinivasan, V. and Weidner, J.W., 2000. Studies on the capacitance of nickel oxide films: effect of heating temperature and electrolyte concentration. *Journal of the Electrochemical Society*, *147*(3), pp.880-885.

113. Lin, C., Ritter, J.A. and Popov, B.N., 1998. Characterization of sol-gel-derived cobalt oxide xerogels as electrochemical capacitors. *Journal of the Electrochemical Society*, *145*(12), pp.4097-4103.

114. Chen, L.Y., Kang, J.L., Hou, Y., Liu, P., Fujita, T., Hirata, A. and Chen, M.W., 2013. High-energy-density nonaqueous MnO_2@ nanoporous gold based supercapacitors. *Journal of Materials Chemistry A*, *1*(32), pp.9202-9207.

115. Trasatti, S. and Kurzweil, P., 1994. Electrochemical supercapacitors as versatile energy stores. *Platinum Metals Review*, *38*(2), pp.46-56.

116. Candler, J., Elmore, T., Gupta, B.K., Dong, L., Palchoudhury, S. and Gupta, R.K., 2015. New insight into high-temperature driven morphology reliant $CoMoO_4$ flexible supercapacitors. *New Journal of Chemistry*, *39*(8), pp.6108-6116.

117. Qu, Q.T., Wang, B., Yang, L.C., Shi, Y., Tian, S. and Wu, Y.P., 2008. Study on electrochemical performance of activated carbon in aqueous Li_2SO_4, Na_2SO_4 and K_2SO_4 electrolytes. *Electrochemistry Communications*, *10*(10), pp.1652-1655.

118. Lisdat, F. and Schäfer, D., 2008. The use of electrochemical impedance spectroscopy for biosensing. *Analytical and Bioanalytical Chemistry*, *391*(5), p.1555-1567.

119. Shaju, K.M., Jiao, F., Débart, A. and Bruce, P.G., 2007. Mesoporous and nanowire Co_3O_4 as negative electrodes for rechargeable lithium batteries. *Physical Chemistry Chemical Physics*, *9*(15), pp.1837-1842.

120. Portet, C., Taberna, P.L., Simon, P. and Flahaut, E., 2005. Influence of carbon nanotubes addition on carbon–carbon supercapacitor performances in organic electrolyte. *Journal of Power Sources*, *139*(1-2), pp.371-378.

121. Hu, C.C. and Chen, W.C., 2004. Effects of substrates on the capacitive performance of $RuO_x \cdot nH_2O$ and activated carbon–RuO_x electrodes for supercapacitors. *Electrochimica Acta*, *49*(21), pp.3469-3477.

122. Zhi, J., Wang, Y., Deng, S. and Hu, A., 2014. Study on the relation between pore size and supercapacitance in mesoporous carbon electrodes with silica-supported carbon nanomembranes. *RSC Advances*, *4*(76), pp.40296-40300.

123. Wang, R., Li, Q., Cheng, L., Li, H., Wang, B., Zhao, X.S. and Guo, P., 2014. Electrochemical properties of manganese ferrite-based supercapacitors in aqueous electrolyte: the effect of ionic radius. *Colloids and Surfaces A: Physicochemical and Engineering Aspects*, *457*, pp.94-99.

124. Vadiyar, M.M., Bhise, S.C., Patil, S.K., Kolekar, S.S., Chang, J.Y. and Ghule, A.V., 2016. Comparative study of individual and mixed aqueous electrolytes with $ZnFe_2O_4$ nano–flakes thin film as an electrode for supercapacitor application. *Chemistry Select*, *1*(5), pp.959-966.

125. Chang, Z., Yang, Y., Li, M., Wang, X. and Wu, Y., 2014. Green energy storage chemistries based on neutral aqueous electrolytes. *Journal of Materials Chemistry A*, *2*(28), pp.10739-10755.

126. Ho, P.C., Palmer, D.A. and Wood, R.H., 2000. Conductivity measurements of dilute aqueous LiOH, NaOH, and KOH solutions to high temperatures and pressures using a flow-through cell. *The Journal of Physical Chemistry B*, *104*(50), pp.12084-12089.

127. Fic, K., Platek, A., Piwek, J. and Frackowiak, E., 2018. Sustainable materials for electrochemical capacitors. *Materials Today*, *21*(4), pp.437-454.